The Astrophysical Journal, 938:84 (21pp), 2022 October 10 https://doi.org/10.3847/1538-4357/ac8c26

Radio Analysis of SN2004C Reveals an Unusual CSM Density Profile as a Harbinger of Core Collapse

Lindsay DeMarchi[1], R. Margutti[2], J. Dittman[3,4], A. Brunthaler[5], D. Milisavljevic[6,7], Michael F. Bietenholz[8], C. Stauffer[1], D. Brethauer[2], D. Coppejans[1,9], K. Auchettl[10,11,12], K. D. Alexander[1], C. D. Kilpatrick[1], Joe S. Bright[2], L. Z. Kelley[1], Michael C. Stroh[1], and W. V. Jacobson-Galán[2]

[1] Center for Interdisciplinary Exploration and Research in Astrophysics and Department of Physics and Astronomy, Northwestern University, 1800 Sheridan Road, Evanston, IL 60208-3112, USA; lindsaydemarchi2024@u.northwestern.edu
[2] Department of Astronomy and Astrophysics, University of California, Berkeley, CA 94720, USA
[3] Center for Astrophysics, Harvard & Smithsonian, 60 Garden Street, Cambridge, MA 02138, USA
[4] Max Planck Institute for Astronomy, Konigstuhl 17, D-69117 Heidelberg, Germany
[5] Max-Planck-Institut für Radioastronomie, Auf dem Hügel 69, 53121 Bonn, Germany
[6] Department of Physics and Astronomy, Purdue University, 525 Northwestern Avenue, West Lafayette, IN 47907, USA
[7] Integrative Data Science Initiative, Purdue University, West Lafayette, IN 47907, USA
[8] Department of Physics and Astronomy, York University, Toronto, M3J 1P3, Ontario, Canada
[9] Department of Physics, University of Warwick, Gibbet Hill Road, Coventry CV4 7AL, UK
[10] Department of Astronomy and Astrophysics, University of California, Santa Cruz, CA 95064, USA
[11] School of Physics, The University of Melbourne, VIC 3010, Australia
[12] ARC Centre of Excellence for All Sky Astrophysics in 3 Dimensions (ASTRO 3D), VIC 3010, Australia
Received 2022 March 14; revised 2022 August 20; accepted 2022 August 22; published 2022 October 14

Abstract

We present extensive multifrequency Karl G. Jansky Very Large Array (VLA) and Very Long Baseline Array (VLBA) observations of the radio-bright supernova (SN) IIb SN 2004C that span ∼40–2793 days post-explosion. We interpret the temporal evolution of the radio spectral energy distribution in the context of synchrotron self-absorbed emission from the explosion's forward shock as it expands in the circumstellar medium (CSM) previously sculpted by the mass-loss history of the stellar progenitor. VLBA observations and modeling of the VLA data point to a blastwave with average velocity ∼0.06 c that carries an energy of $\approx 10^{49}$ erg. Our modeling further reveals a flat CSM density profile $\rho_{\rm CSM} \propto R^{-0.03\pm0.22}$ up to a break radius $R_{\rm br} \approx (1.96 \pm 0.10) \times 10^{16}$ cm, with a steep density gradient following $\rho_{\rm CSM} \propto R^{-2.3\pm0.5}$ at larger radii. We infer that the flat part of the density profile corresponds to a CSM shell with mass ∼0.021 $M_\odot$, and that the progenitor's effective mass-loss rate varied with time over the range $(50\text{–}500) \times 10^{-5}\, M_\odot\ {\rm yr}^{-1}$ for an adopted wind velocity $v_w = 1000\ {\rm km\,s^{-1}}$ and shock microphysical parameters $\epsilon_e = 0.1$, $\epsilon_B = 0.01$. These results add to the mounting observational evidence for departures from the traditional single-wind mass-loss scenarios in evolved, massive stars in the centuries leading up to core collapse. Potentially viable scenarios include mass loss powered by gravity waves and/or interaction with a binary companion.

Key words: Core-collapse supernovae – Stellar mass loss – Circumstellar shells – Circumstellar matter – Supernovae – Radio astronomy

1. Introduction

All stars lose mass to their environments throughout their lifetimes, critically affecting both the star's evolution and fate in addition to enriching the universe with heavy elements. If the star dies in a supernova (SN) explosion, shock interaction with recent mass lost to the circumstellar medium shapes the appearance of the SN display.

In recent years, observations of SNe have uncovered evidence that evolved massive stars live complex lives with a rich and diverse mass-loss history, particularly in the final moments before their deaths. Large optical data sets that sampled the pre-explosion phase of SNe (such as the targets observed by the Palomar Transient Factory, PTF, and the Zwicky Transient Facility; Law et al. 2009; Bellm et al. 2019; Graham et al. 2019) have unveiled evidence of pre-explosion eruptions in >50% of progenitors of Type IIn SNe (Ofek et al. 2014; later updated by Strotjohann et al. 2021), which are SNe that explode into dense H-rich circumstellar medium (CSM) and show narrow hydrogen lines in their spectra as a consequence (Filippenko 1997). Among Type IIn SNe, the precursor event of SN 2010mc (Ofek et al. 2013) and the long history of pre-SN eruptions of SN 2009ip (Smith et al. 2010; Foley et al. 2011) were among the first events inferring the presence of a dense CSM shell extending $\sim 5 \times 10^{14} - \sim 4 \times 10^{16}$ cm from their explosion sites. The existence of these shells points to a mass-loss mechanism different from the traditional line-driven winds, and hence exposes gaps in our understanding of massive stellar evolution (Fraser et al. 2013; Mauerhan et al. 2013; Pastorello et al. 2013; Prieto et al. 2013; Margutti et al. 2014; Mauerhan et al. 2014; Smith & Arnett 2014). Interestingly, evidence of large mass-loss events (0.01 to several $M_\odot$ lost to the environment) occurring in the centuries to years before death extends to the H-rich progenitors of superluminous SNe (SLSNe-II), a class assigned to SNe orders of magnitude more luminous than normal ones that also show H in early spectra. SN 2008es is one such example, which interacted with 2–3 $M_\odot$ material 0.5–1.6 yr prior to explosion (Bhirombhakdi et al. 2019).

Importantly, violent pre-SN mass loss is not strictly limited to H-rich progenitors. Revealed by an increasing wealth of multiwavelength observational evidence, H-*poor* progenitors of

SNe Type IIb and Type Ib/c (SN Ib/c) exhibit enhanced mass loss prior to explosion as well (see, e.g., Benetti et al. 2018; Kuncarayakti et al. 2018; Mauerhan et al. 2018; Gomez et al. 2019; Kundu et al. 2019; Prentice et al. 2020; Jacobson-Galán et al. 2020, 2021; Gutiérrez et al. 2021; Jin et al. 2021; Maeda et al. 2021, for recent examples). A new class of SN explosion that shows interaction with a H-poor environment is Type Icn (SN Icn; Fraser et al. 2021; Perley et al. 2022; Gal-Yam et al. 2021). This phenomenon also extends to H-poor SLSNe (SLSNe-I). For example, iPTF13ehe, iPTFesb, iPTF16bad, iPTF16eh, SN 2018bsz, and other events discussed in Hosseinzadeh et al. (2022) show evidence of CSM material located $\sim 10^{16}$ cm from their explosion sites (Yan et al. 2017; Anderson et al. 2018; Lunnan et al. 2018; Chen et al. 2021; Pursiainen et al. 2022).

Radio observations of SNe played a key role in our understanding of "unusual" CSM density profiles around SNe (e.g., Chevalier & Fransson 2017 for a recent review). In an SN explosion, while optical observations sample the slowly expanding ejecta ($v \leqslant 10^4$ km s^{-1}), radio observations probe the fastest ejecta ($v \geqslant 0.1c$). Radio synchrotron emission originates from the interaction of the fastest SN ejecta with the local CSM deposited by the progenitor star prior to explosion. By monitoring the temporal evolution of the spectral peak frequency and flux density, one may directly constrain physical properties of the system, such as the mass-loss rate $\dot{M}$ of the progenitor star. Therefore, radio observations allow us to map the density profile of the CSM around the explosion site. Previous works in the literature have built a foundation of using this approach to measure pre-explosion mass loss of H-stripped progenitors at radio frequencies as the blastwave interacts with the surrounding CSM (see, e.g., SNe 2001ig, 2001em, 2003bg, 2003gk, 2007bg, 2008ax, and PTF11qcj; Ryder et al. 2004; Soderberg et al. 2006; Roming et al. 2009; Schinzel et al. 2009; Salas et al. 2013; Bietenholz et al. 2014; Corsi et al. 2014). Using the standard techniques of radio analysis and radio data modeling (as reviewed in Weiler et al. 2002; Chevalier & Fransson 2017), we have found that SN 2004C is one of such H-poor explosions with a shockwave that encounters a dense CSM with a profile that is not consistent with the traditional single stellar wind models.

Observations across the electromagnetic spectrum of SNe thus point to the presence of strongly time-dependent mass loss predicating core collapse in a diversity of explosion types, ranging from stripped-envelope SNe Ib/c to SNe II and extending to SLSNe. The fact that these mass-loss ejections occur across different types of SNe implies an origin of the outbursts that is independent of progenitor size. The exact nature of the underlying physical process causing this time-dependent mass loss remains the subject of debate, as well as how these processes inform the evolutionary path of the progenitor (e.g., Smith 2014).

In this work we analyze the radio data of SN 2004C, an SN Type IIb that exploded 2003 December 15 (MJD 52988; see Section 2.1) located in the galaxy NGC 3683, 35.9 Mpc away (Dudley & Fischer 2004; Tully et al. 2009, 2013). Our radio data set spans 40–2793 days post-explosion and represents one of the most extensive radio data sets of an SN thus far, which we model with synchrotron self-absorption. Furthermore, Very Long Baseline Array (VLBA) imaging of SN 2004C at 1931 days post-explosion offers a direct measurement of the blastwave radius, making SN 2004C among the ~10 SN with published VLBA constraints to date. With the use of our generalized equations from Chevalier (1998, hereafter C98), we find the explosion site of SN 2004C contains a dense shell of CSM material, and we speculate on its physical origin.

Our paper is organized as follows. The VLA and VLBA data of SN 2004C are presented in Section 2, and our generalization of the equations following the formalism of C98 is in Section 3. Our modeling of the data and analysis of the physical parameters of the system are presented in Section 4. Our comparison to plausible mass-loss mechanisms is presented in Section 5, and we summarize our results in Section 6.

2. Observations

2.1. Explosion Date and SN Typing

SN 2004C was discovered 2004 January 12.5 UT in near-infrared K'-band (2.1 μm) imaging with relatively poor constraints on the time of explosion (Dudley & Fischer 2004). The most recent prior observation of that region was taken 2003 May 18 and published photometry are insufficient to robustly constrain the time of maximum light and potentially extrapolate an explosion date. The only known attempt was made by Meikle et al. (2004), who estimated that SN 2004C was 3 weeks past maximum light as of 2004 January 16 by comparing its $g' - r'$ and $r' - i'$ colors to those of Type Ic supernovae. That estimate, however, is problematic given that years later Shivvers et al. (2017) reported that the spectral classification of SN 2004C was in fact Type IIb, and not Type Ic as originally reported (Matheson et al. 2004).

To better estimate the date of explosion, we supplemented these reports and the updated spectroscopic classification with our own investigation of archival optical spectra of SN 2004C retrieved from WISeREP (Yaron & Gal-Yam 2012). Spectra spanned 2004 January 16 to March 17, and were inspected for their likeness to other Type IIb spectra tagged with time since explosion and/or maximum light. Our comparisons were aided with use of `SNID` (Blondin & Tonry 2007); we heavily weighted a high-quality Lick 3 m spectrum of SN 2004C obtained 2004 January 17 and originally published in Shivvers et al. (2017) in our manual comparisons. Among all Type IIb supernova spectra inspected, those of SN 1993J and SN 2000H displayed the closest similarity in spectral evolution with the limited available epochs of SN 2004C. Comparisons converged on the time of maximum light of SN 2004C to be around 2004 January 2. Given an average Type IIb V-band rise-to-peak time of approximately 18 days from explosion (see, e.g., Milisavljevic et al. 2013), we estimate the explosion date to be 2003 December 15 with an uncertainty of ~ 2 weeks dominated by ambiguity between fits with other epochs. In the following we adopt MJD 52988 (corresponding to 2003 December 15) as the explosion date. This uncertainty has no impact on our major conclusions.

2.2. Karl G. Jansky Very Large Array

We observed SN 2004C with the NSF's Karl G. Jansky Very Large Array (VLA) beginning on 2004 January 23.65 UT, $\delta t \approx 30$ days after the initial discovery under programs AK0575 and AS0796 (PI Soderberg). We found a radio source at $\alpha = 11^{\rm h}27^{\rm m}29\overset{\rm s}{.}72$, $\delta = +56^\circ 52' 48\overset{''}{.}2$, coincident with the optical SN position with a flux density of $F_\nu = 1.6 \pm 0.05$ mJy at a frequency of $\nu = 8.5$ GHz. We continued to monitor this source for the next $\delta t \approx 2800$ days.

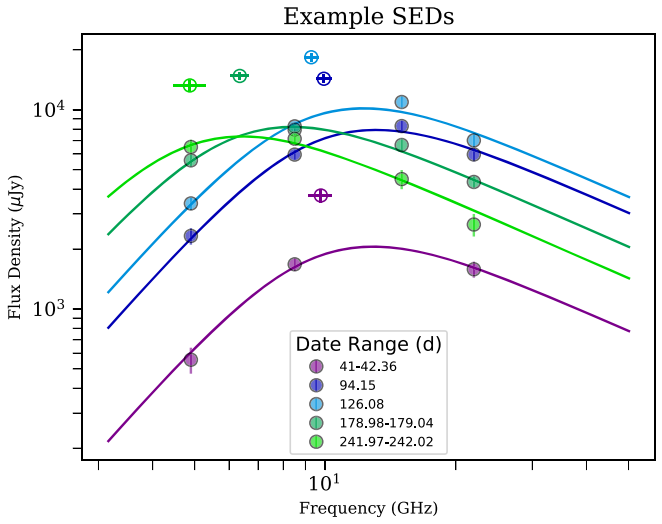

Figure 1. A few example radio SEDs are chosen to show the evolution of the emission through time. Note that for SN 2004C, the evolution of the peak flux density and peak frequency does not follow a power law with time and our modeling is designed to adapt to this nonstandard evolution. Solid lines: best-fitting model. Solid points: radio observations of SN 2004C. Hollow points: intercepts of the asymptotic power-law segments, which mark the location of $\nu_{\rm brk}$ and $F_{\rm brk}$. These values are used to estimate the physical properties of the SN outflow and its environment.

Radio data were taken in the 4.9, 8.5, 15.0, and 22.0 GHz bands, and we give the measured flux densities in Table 3. Observations were taken in continuum observing mode with 2×50 MHz bandwidth, except that in 2011 August, which was taken with the upgraded EVLA system, with an increased 2 GHz bandwidth. We used observations of J1127+568 to calibrate the time-dependent complex gains of the instrument and 3C286 to calibrate the absolute flux scale and the bandpass response for all observations. Data were reduced using the Astronomical Image Processing System (AIPS) by fitting an elliptical Gaussian model to the radio SN in each observation to measure the integrated flux density. We note that that SN 2004C has a peak luminosity density at 100 days of $\sim 10^{28}$ erg s^{-1} Hz^{-1} and is at the high end of the radio luminosity function for SNe (see, e.g., Bietenholz et al. 2021). A subsection of data points showcasing the SN evolution is shown in Figure 1, and the full data set is plotted in Appendix D, Figure 10. In Figure 2, we show the light curves for SN 2004C at 4.9, 8.5, 15.0, and 22.0 GHz bands.

Temporally, the radio flux density at 8.5, 15.0, and 22.0 GHz rises slowly over the first 100 days and then steadily declines. At 4.9 GHz, the radio flux density increases for approximately the first 200 days, peaking at 10 mJy, and then plateaus for several hundred more days until beginning to decline. We see evidence for a low-frequency turnover in our spectral energy distribution, which is readily apparent in Figure 10 of Appendix D, as well as in the raw radio light curves in Figure 2.

2.3. Very Long Baseline Array

We observed SN 2004C with the NRAO VLBA as part of program BS192 (PI Soderberg) on 2009 March 29 at 8.4 GHz. The observations were performed with eight frequency bands of 8 MHz bandwidth each in dual circular polarization, resulting in a total data rate of 512 Mbps. ICRF J112813.3+592514, located at $\alpha_{2000} = 11^{\rm h}28^{\rm m}13\overset{\rm s}{.}3406$ and $\delta_{2000} = +59°25'14\overset{''}{.}798$ (Fey et al. 2004) was used for phase-referencing at both frequencies. We cycle time of ∼5 minutes, with ∼4 minutes on SN 2004C and 1 minutes on ICRF J112813.3+592514, and the total length of the observations was 8 hr.

The data were correlated at the VLBA Array Operations Center in Socorro, New Mexico and calibrated using AIPS and ParselTongue (Kettenis et al. 2006). Total electron content maps of the ionosphere were used to correct for ionospheric phase changes. Amplitude calibration used system temperature measurements and standard gain curves. We performed a "manual phase-calibration" using the data from one scan of J112813.3+592514 to remove instrumental phase offsets among the frequency bands. We then fringe-fitted the data from ICRF J112813.3+592514. Finally, the calibration was transferred to SN 2004C. The data were imaged in AIPS using robust weighting (with AIPS `ROBUST = 0`). We clearly detect the source with an integrated flux density of $F_\nu = 0.74 \pm 0.13$ mJy at coordinates $\alpha = 11^{\rm h}27^{\rm m}29\overset{\rm s}{.}728309 \pm 0\overset{\rm s}{.}000012$, $\delta = 56°52'48\overset{''}{.}12937 \pm 0\overset{''}{.}00014$. The beam size of our observation is ≈3 mas, and the source is clearly resolved in our data with a size of $0.707^{+0.120}_{-0.178}$ mas ($3.8^{+0.6}_{-1.0} \times 10^{17}$ cm at 35.9 Mpc). The total clean flux density in the VLBI image, $F_\nu = 0.74 \pm 0.13$ mJy is consistent with our VLA flux density measurement taken on 2009 April 5.22 UT (7 days after the VLBA measurement) of 0.72 ± 0.07 mJy (Table 3).

3. Radio Modeling

3.1. Radio Synchrotron Emission in SNe: Emitting Radius R, Post-shock Magnetic Field B, and Energy U

In an SN explosion, the propagation of the fastest ejecta into the environment creates a double-shock structure: one shock propagates outward (the forward shock, FS) and the other propagates inward in mass coordinates into the SN ejecta (the reverse shock, or RS). The two shocked regions of CSM and SN ejecta are separated by a contact discontinuity.

Radio emission in young nonrelativistic SNe is dominated by synchrotron radiation from electrons accelerated at the FS (e.g., Chevalier 1998; Weiler et al. 2002; Chevalier & Fransson 2017). Relativistic electrons gyrate in a magnetic field B with pitch angle θ in the shocked CSM and radiate photons as nonthermal synchrotron emission (Rybicki & Lightman 1986). The acceleration of these electrons creates a power-law distribution in electron Lorentz factor γ_e, where $dN(\gamma_e)/d\gamma_e = K_0 \gamma_e^{-p}$ for $\gamma_e \geqslant \gamma_{\rm m}$, where $\gamma_{\rm m}$ is the minimum Lorentz factor. Here, N is the number of electrons per unit volume, K_0 is the normalization constant, and p is the power-law index of the electron distribution.[13] Therefore, the typical electron Lorentz factor of the power-law distribution is $\gamma_e \approx \gamma_{\rm m}$. Radio observations of SNe typically indicate $p \approx 3$ (e.g., Berger et al. 2002; Weiler et al. 2002; Soderberg et al. 2004, 2006c; Chevalier & Fransson 2006; Soderberg et al. 2006, 2006, 2007, 2010a, 2010b, 2012; Corsi et al. 2014, 2016; Kamble et al. 2016, for observational results, and a theoretical basis is given in Diesing & Caprioli 2021). Diversity among the values of p in SN explosions might be a manifestation of different physical properties in the shocks where particle acceleration happens.

The resulting radio flux density spectrum, F_ν, is a series of broken power laws (BPLs) with spectral breaks that occur at frequencies and flux densities set by the physical properties of

[13] We note that the power-law variable p is sometimes expressed as γ in the radio SN literature. However, we wish to avoid confusion with the electron Lorentz factor, and adopt p instead.

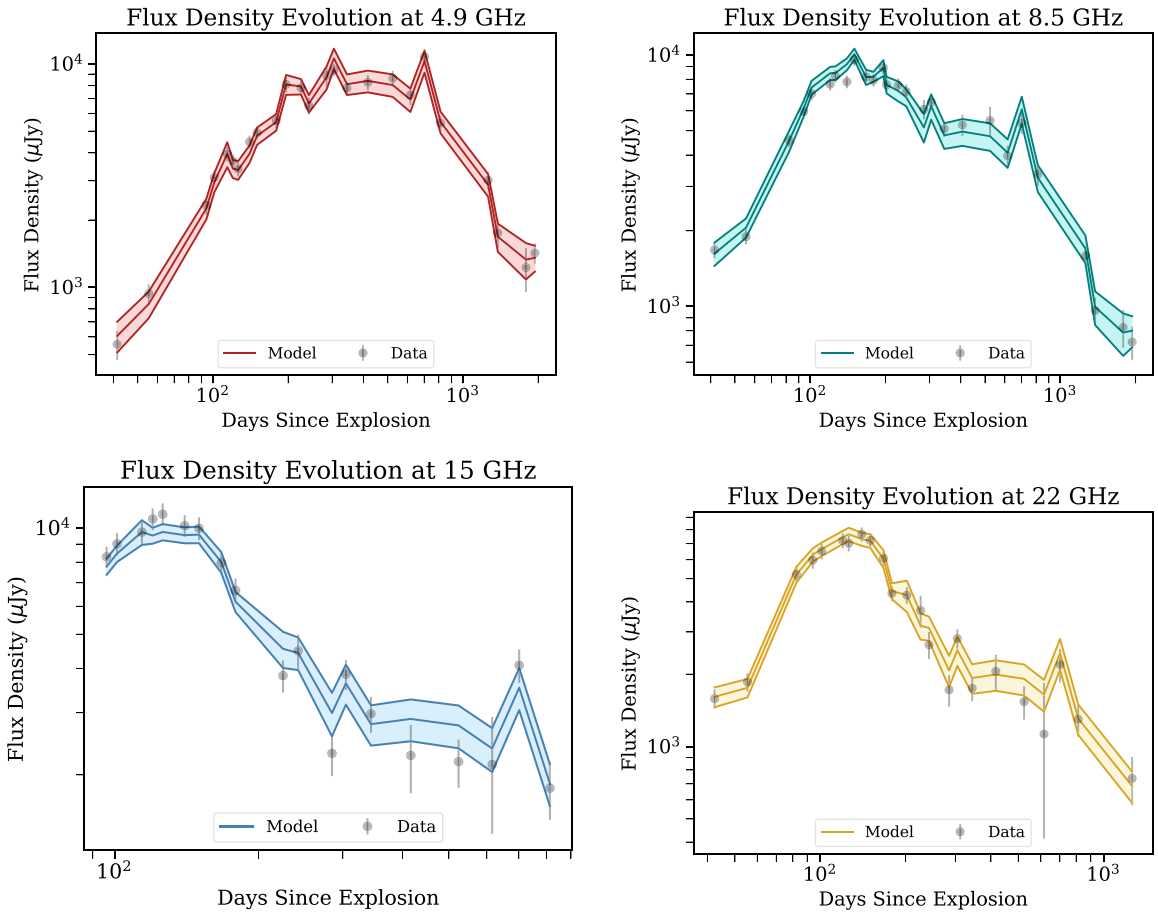

Figure 2. Light curves of SN 2004C data at 4.9, 8.5, 15, and 22 GHz (gray points). Overlaid is our model fit to the data; shaded regions represent the spread of the 1σ uncertainty on the broken power-law (BPL) fit parameters (Table 1).

the system (e.g., B, electron density n_e, etc.). Notable break frequencies are the synchrotron cooling frequency, ν_c, the synchrotron characteristic frequency, $\nu_{\rm m}$, and the synchrotron self-absorption frequency, $\nu_{\rm sa}$. The slopes of F_ν power-law segments depend on the order of ν_c, $\nu_{\rm m}$, and $\nu_{\rm sa}$ (e.g., Figure 1 of Granot & Sari 2002).

We further define the shock microphysical parameters ϵ_B and ϵ_e as the fraction of the energy density $\frac{2}{1+i}\rho_{\rm CSM}v^2$ that goes into the post-shock magnetic field energy density E_B and the relativistic electron energy density E_e. We introduce the numerical factor i to parameterize the different definitions of the reference energy density that appear in the literature (see Appendix C for details). For our modeling, we keep the dependence on i explicit. For reference, the traditional parameterization of C98 corresponds to $i=1$. We note that in the SN literature, there are at least three other definitions of the shock microphysical parameters that we discuss in detail in Appendix C. It is important to keep in mind that these different definitions lead to different values of inferred parameters (most notably the mass loss, $\dot{M}$) even when the same shock microphysical parameters values are assumed (Section 3.2), as we also show in Appendix C. The energy densities are defined as follows:

$$E_B \equiv \frac{B^2}{8\pi} = \left(\frac{2}{1+i}\right)\epsilon_B \rho_{\rm CSM} v^2 \tag{1}$$

and

$$E_e \equiv \int_{\gamma_m}^{\infty} (\gamma_e m_e c^2) K_0 \gamma_e^{-p} d\gamma_e = \left(\frac{2}{1+i}\right)\epsilon_e \rho_{\rm CSM} v^2, \tag{2}$$

where $\rho_{\rm CSM}$ is the *unshocked* CSM density and $v \equiv dR/dt$ is the FS velocity.

The frequency above which electrons cool efficiently through synchrotron radiation over a dynamical timescale $t_{\rm dyn}$ is ν_c, defined as (Rybicki & Lightman 1986):

$$\nu_c \equiv \frac{18\pi m_e c e}{t_{\rm dyn}^2 \sigma_T^2 B^3}, \tag{3}$$

where σ_T is the Thomson cross section, m_e is the mass of the electron, e is the charge of the electron, and c is the speed of light, all in c.g.s. units. For our purposes, $t_{\rm dyn}$ can be identified as the time since the SN explosion. In radio SNe, $B \equiv B(t)$, which adds another dependency of ν_c on time.

The single-electron synchrotron spectrum F_ν peaks at $\nu = \gamma_e^2(\frac{eB}{2\pi m_e c})$ (e.g., Rybicki & Lightman 1986), which allows us to define the characteristic synchrotron frequency:

$$\nu_{\rm m} \equiv \gamma_m^2 \left(\frac{eB}{2\pi m_e c}\right). \tag{4}$$

Following Soderberg (2007), under the assumptions that particle kinetic energy is conserved across the shock

discontinuity and a pure H composition:

$$\epsilon_e (v/c)^2 m_p c^2 \approx \bar{\gamma} m_e c^2, \quad (5)$$

where $\bar{\gamma}$ is the average electron Lorentz factor and m_p is the proton mass. For a $dN/d\gamma_e$ power-law distribution of electrons, $\bar{\gamma} \approx \gamma_m$, which, substituting into Equation (4), leads to:

$$\nu_{\rm m} \approx \epsilon_e^2 \left(\frac{v}{c}\right)^4 \left(\frac{m_p}{m_e}\right)^2 \left(\frac{eB}{2\pi m_e c}\right). \quad (6)$$

For typical radio SN parameters (e.g., from Soderberg et al. 2006), $B \sim 1$ G, $v \sim 0.1\,c$, it follows from Equations (3) and (6) that $\nu_c \gtrsim 100$ GHz and $\nu_{\rm m} \ll 1$ GHz. Taking SN 2003bg as an example, at $t^* \approx 35$ d since explosion, Soderberg et al. (2006) infer $v(t^*) \approx 0.13\,c$ and $B(t^*) \approx 0.9$ G, which implies $\nu_{\rm m}(t^*) \approx 2.5(\epsilon_e/0.1)^2 \times 10^{-2}$ GHz and $\nu_c(t^*) \approx 2.6 \times 10^2$ GHz. It follows that for young radio SNe $\nu_{\rm m} < \nu_c$ and the only relevant spectral break frequency that typically enters the 0.1–100 GHz radio spectrum is $\nu_{\rm sa}$.

$\nu_{\rm sa}$ divides the radio spectrum into optically "thick" ($F_{\nu,\rm thick}$, for $\nu < \nu_{\rm sa}$), and optically "thin" ($F_{\nu,\rm thin}$, for $\nu > \nu_{\rm sa}$). At frequencies below $\nu_{\rm sa}$, the optical depth to synchrotron emission is $\tau_{\rm sa}(\nu_{\rm sa}) > 1$, and in the absence of any other absorption mechanism, synchrotron self-absorbed emission (SSA) dominates (Rybicki & Lightman 1986). In the spectral regime of interest, $F_{\nu,\rm thick} \propto \nu^{5/2}$ for $\nu_{\rm m} < \nu < \nu_{\rm sa}$. We note for completeness that at lower frequencies $\nu < \nu_{\rm m} < \nu_{\rm sa}$, $F_{\nu,\rm thick} \propto \nu^2$ (e.g., Granot & Sari 2002).

In order to derive physical quantities from a single SED, we follow Rybicki & Lightman (1986) and C98. The specific intensity I_ν can be expressed as follows:

$$I_\nu = S_\nu(\nu_{\rm sa}) J_\nu(y, p), \quad (7)$$

where

$$S_\nu(\nu_{\rm sa}) = \frac{c_5}{c_6} (B \sin\theta)^{-1/2} \left(\frac{\nu_{\rm sa}}{2c_1}\right)^{5/2}, \quad (8)$$

$$\nu_{\rm sa} = 2c_1 \left[\frac{4}{3} f R c_6\right]^{2/(p+4)} N_0^{2/(p+4)} (B \sin\theta)^{(p+2)/(p+4)}, \quad (9)$$

$$J_\nu(y, p) = y^{5/2}(1 - e^{-y^{-(p+4)/2}}), \quad (10)$$

and $y \equiv \frac{\nu}{\nu_{\rm sa}}$. The constant c_1 and the parameters $c_5(p)$, and $c_6(p)$ are defined in Pacholczyk (1970) and provided in full in Appendix A. As these parameters are functions of p, it is typical in the radio SN literature to approximate $c_5 \sim c_5(p = 3)$ and $c_6 \sim c_6(p = 3)$, irrespective of what the best-fitting p is for the SED. In this work we self-consistently account for the dependency of c_5 and c_6 on the electron power-law index p. Additionally, we leave $B \sin\theta$ explicit in our derivation (as opposed to approximating $B \sin\theta \approx B$), as further physical quantities will not maintain the same exponential relationships between B and $\sin\theta$.[14] In Equations (7), (8), and (10) above, the radio emitting region is assumed to be a disk in the sky of radius R, thickness s, and volume $V = \pi R^2 s$. The filling factor f is the fractional volume of a sphere of radius R such that the emitting volume is

$$V = \pi R^2 s \equiv f \times 4/3 \pi R^3. \quad (11)$$

Canonically, a value $f = 0.5$ is adopted, but we leave f explicit in this work. The number density distribution of relativistic electrons per unit volume in energy space can be expressed as $dN/dE = N_0 E^{-p}$, with N_0 as the normalization. This relates to K_0 through $K_0 \gamma_e^{-p} d\gamma_e = N_0 E^{-p} dE$ and $E = \gamma_e m_e c^2$. Following Equation (2), $E_e = \int_{E_l}^{\infty} E\, N_0 E^{-p}\, dE = \int_{\gamma_m}^{\infty} (\gamma_e m_e c^2) K_0 \gamma_e^{-p} d\gamma_e$ and E_l is the lowest energy of the electrons accelerated to a power law, $E_l = \gamma_m m_e c^2$. For $p > 2$, the energy density in relativistic electrons of Equation (2) can be also expressed as

$$E_e = (N_0 E_l^{2-p})/(p - 2). \quad (12)$$

We may now express the way Equation (12) relates to B:

$$\frac{1}{\epsilon_B} \frac{B^2}{8\pi} = \frac{1}{\epsilon_e} \frac{N_0 E_l^{(2-p)}}{(p - 2)}. \quad (13)$$

The flux density F_ν of a source of radial extent R and constant I_ν over the subtended solid angle, $\Omega = \pi R^2/D^2$ is $F_\nu = I_\nu \pi R^2/D^2$, where D is the distance of the source.

Considering the asymptotic limits $\nu \gg \nu_{\rm sa}$ (optically thick) and $\nu \ll \nu_{\rm sa}$ (optically thin), and using the equations above, C98 derives:

$$F_{\nu,\rm thick}(\nu) = \frac{c_5}{c_6} (B \sin\theta)^{-\frac{1}{2}} \left(\frac{\nu}{2c_1}\right)^{\frac{5}{2}} \frac{\pi R^2}{D^2}, \quad (14)$$

which scales as $F_{\nu,\rm thick} \propto \nu^{5/2}$, and the optically thin flux density $F_{\nu,\rm thin} \propto \nu^{-(p-1)/2}$ is:

$$F_{\nu,\rm thin}(\nu) = c_5 \left(\frac{\nu}{2c_1}\right)^{\frac{-(p-1)}{2}} (B \sin\theta)^{\frac{p+1}{2}} N_0 \frac{4}{3} \pi f \frac{R^3}{D^2}. \quad (15)$$

We define a break frequency parameter $\nu_{\rm brk}$ as the spectral frequency at which the asymptotically thick and thin flux densities (Equations (14) and (15)) meet: $F_{\nu,\rm thin}(\nu_{\rm brk}) = F_{\nu,\rm thick}(\nu_{\rm brk}) \equiv F_{\rm brk}$. After combining Equations (13), (14), and (15) and solving for B and R, we find the results below. We provide coefficients containing several digits to avoid rounding errors if a reader were to use these equations as provided.

$$B = (2.50 \times 10^9) \left(\frac{\nu_{\rm brk}}{5\ {\rm GHz}}\right) \left(\frac{1}{c_1}\right) \times \left[\frac{4.69 \times 10^{-23} \left(\frac{E_l}{\rm erg}\right)^{2(2-p)} \epsilon_B^2 c_5 \sin(\theta)^{\frac{1}{2}(-5-2p)}}{(p - 2)^2 \left(\frac{D}{\rm Mpc}\right)^2 \epsilon_e^2 \left(\frac{f}{0.5}\right)^2 \left(\frac{F_{\rm brk}}{\rm Jy}\right) c_6^3}\right]^{\frac{2}{13+2p}} {\rm G}, \quad (16)$$

[14] See Yang & Zhang (2018) for a recent discussion regarding the flux density dependence on the pitch angle θ distribution of the radiating electrons.

$$R = (2.50 \times 10^{9})^{-1} c_1 \left(\frac{\nu_{\rm brk}}{5\ {\rm GHz}}\right)^{-1} \Bigg[12 \epsilon_B c_5^{-(6+p)} c_6^{(5+p)} \times (9.52 \times 10^{25})^{(6+p)} \sin^2\theta \pi^{-(5+p)} \left(\frac{D}{\rm Mpc}\right)^{2(6+p)} \times \left(\frac{E_l}{\rm erg}\right)^{(2-p)} \left(\frac{F_{\rm brk}}{\rm Jy}\right)^{(6+p)} \times \left(\epsilon_e (p-2) \left(\frac{f}{0.5}\right)\right)^{-1} \Bigg]^{1/(13+2p)} {\rm cm}. \quad (17)$$

For direct comparison to C98, we evaluate B and R at typical values of the physical parameters for radio SNe, i.e., $p = 3$, $E_l = m_e c^2$, and $\sin\theta \approx 1$ (e.g., Berger et al. 2002; Weiler et al. 2002; Chevalier & Fransson 2006; Soderberg et al. 2006; Corsi et al. 2014). Below, we demonstrate that Equation (16) reduces to Equation (12) in C98, and Equation (17) reduces to their Equation (11):

$$B = 0.5761 \left(\frac{\nu_{\rm brk}}{5\ {\rm GHz}}\right) \times \left[\epsilon_B^{-1} \left(\frac{D}{\rm Mpc}\right) \epsilon_e \left(\frac{f}{0.5}\right) \left(\frac{F_{\rm brk}}{\rm Jy}\right)^{1/2}\right]^{-4/19} {\rm G}, \quad (18)$$

$$R = 8.759 \times 10^{15} \left(\frac{\nu_{\rm brk}}{5\ {\rm GHz}}\right)^{-1} \times \left[\left(\frac{D}{\rm Mpc}\right)^{18} \epsilon_B \left(\frac{F_{\rm brk}}{\rm Jy}\right)^{9} \epsilon_e^{-1} \left(\frac{f}{0.5}\right)^{-1}\right]^{1/19} {\rm cm}. \quad (19)$$

From Equations (1), (11), (16), and (17), the post-shock energy corresponding to the energy density $\frac{2}{1+i}\rho_{\rm CSM} v^2$ is $U \equiv (\frac{2}{1+i}\rho_{\rm CSM} v^2) \times V = B^2/(\epsilon_B 8\pi) \times (4/3\pi R^3 f)$, or:

$$U = c_1 (3.33 \times 10^{-11}) \epsilon_B^{-1} 10^{\frac{75(6+p)}{13+2p}} \times \left(\frac{f}{0.5}\right) \left(\frac{\nu_{\rm brk}}{5\ {\rm GHz}}\right)^{-1} \Bigg[3.086^{6(6+p)} 4.411 \times 10^{-96} \times \left(\frac{D}{\rm Mpc}\right)^{28+6p} \left(\frac{F_{\rm brk}}{\rm Jy}\right)^{14+3p} \pi^{-3(1+p)} \sin\theta^{-4(1+p)} \times c_5^{-(14+3p)} c_6^{3(1+p)} (2\epsilon_B \epsilon_e^{-1} (p-2)^{-1} \times \left(\frac{E_l}{\rm erg}\right)^{2-p} \left(\frac{f}{0.5}\right)^{-1}\Bigg)^{11} \Bigg]^{1/(13+2p)} {\rm erg}. \quad (20)$$

We note that for the case of a monatomic gas and a strong shock, the post-shock thermal energy is $U_{\rm th} = \frac{9}{8} V \rho_{\rm CSM} v^2$ (e.g., Petropoulou et al. 2016; see Appendix C for a comparison).

Substituting $p = 3$, $E_l = m_e c^2$, and $\sin\theta \approx 1$ as above, our Equation (21) reduces to Equation (12) in Ho et al. (2019):

$$U = 1.859 \times 10^{46} \epsilon_B^{-1} \left(\frac{\nu_{\rm brk}}{5\ {\rm GHz}}\right)^{-1} \times \left[\epsilon_B^{11} \epsilon_e^{-11} \left(\frac{f}{0.5}\right)^{8} \left(\frac{D}{\rm Mpc}\right)^{46} \left(\frac{F_{\rm brk}}{\rm Jy}\right)^{23}\right]^{1/19} {\rm erg}. \quad (21)$$

3.2. Radio Synchrotron Emission in SNe: Environment Density ρ_{CSM} and Pre-explosion Mass-loss Rate $\dot{M}$

A physical quantity of interest is the density of matter in the pre-shocked circumstellar medium, which directly traces the mass-loss history of the progenitor system before the star's death. We derive the density of the unshocked CSM, $\rho_{\rm CSM}$, by rearranging Equation (1) and substituting for B and R (Equations (16) and (17)). Additionally, we follow C98 in assuming the evolution of the shock radius with time follows a power law $R \propto t^q$ (either globally or locally), such that $v \equiv dR/dt = qR/t$ (see Appendix C, and $R(t)$ in Figure 3 for an example). Thus,

$$\rho_{\rm CSM} = 5.8 \times 10^{45} \left(\frac{\nu_{\rm brk}}{5{\rm GHz}}\right)^{4} \left(\frac{t}{\rm days}\right)^{2} (i+1) \times (c_1^4 \epsilon_B q^2)^{-1} \Bigg[3.355 \times 10^{-92} \times 10^{-50(6+p)} \times 3.086^{-4(6+p)} c_5^{2(8+p)} c_6^{-2(11+p)} \times \left(\frac{D}{\rm Mpc}\right)^{-4(8+p)} \left(\frac{F_{\rm brk}}{\rm Jy}\right)^{-2(8+p)} \pi^{2(5+p)} \sin(\theta)^{-2(7+2p)} \times \left[\left(\frac{E_l}{\rm erg}\right)^{(p-2)} \epsilon_B^{-1} \epsilon_e \left(\frac{f}{0.5}\right)(p-2)\right]^{-6} \Bigg]^{\frac{1}{(13+2p)}} {\rm g\ cm^{-3}}. \quad (22)$$

For a shock that originates from the interaction between the outer layers of dense SN ejecta (which has a power-law distribution of density in radius $\rho_{\rm ej} \propto R^{-n}$) and a power-law density distribution of CSM ($\rho_{\rm CSM} \propto R^{-s}$), the shock radius evolution is described by the self-similar solutions in Chevalier (1982).[15] $R(t) \propto t^{\frac{n-3}{n-s}}$, which implies $q = \frac{n-3}{n-s}$. We note this relationship only holds in the regime of the self-similar solution, i.e., so long as $n > 5$ and $s < 3$ (Chevalier 1982). For a core-collapse SN originating from a compact, massive, stripped progenitor such as a Wolf–Rayet (WR) star $n \approx 10$, and the CSM created from massive stellar winds scales with $s = 2$, which leads to a value of $q = 7/8$ that is typically applied in the literature (see, e.g., Chevalier & Fransson 2006). From Equation (22), and a radio spectrum, the inferred pre-shock CSM density scales as $\rho_{\rm CSM} \propto \frac{1+i}{q^2}$.

Introducing the mean molecular weight per electron parameter μ_e and proton mass m_p for the CSM, the electron number density in the unshocked CSM is $n_e = \frac{\rho_{\rm CSM}}{m_p \mu_e}$, or:

$$n_e = 5.8 \times 10^{45} (i+1) \left(\frac{\nu_{\rm brk}}{5{\rm GHz}}\right)^{4} \left(\frac{t}{\rm days}\right)^{2} (c_1^4 \epsilon_B m_p \mu_e q^2)^{-1} \times [3.355 \times 10^{-92} \times 10^{-50(6+p)} \times 3.086^{-4(6+p)} c_5^{2(8+p)} c_6^{-2(11+l} \times \left(\frac{D}{\rm Mpc}\right)^{-4(8+p)} \left(\frac{F_{\rm brk}}{\rm Jy}\right)^{-2(8+p)} \pi^{2(5+p)} \sin(\theta)^{-2(7+2p)} \times \left[\left(\frac{E_l}{\rm erg}\right)^{(p-2)} \epsilon_B^{-1} \epsilon_e \left(\frac{f}{0.5}\right)(p-2)\right]^{-6}\Bigg]^{1/(13+2p)} {\rm cm^{-3}}. \quad (23)$$

During its lifetime, a star loses material to its surroundings and sits in a polluted environment of its own debris. For stars that lose mass through a constant mass-loss rate $\dot{M}$ and wind

[15] The power-law density of the unshocked medium, s, is not to be confused with the model smoothing parameter s in Section 3.3. We use this notation for ease of comparison to Chevalier (1982).

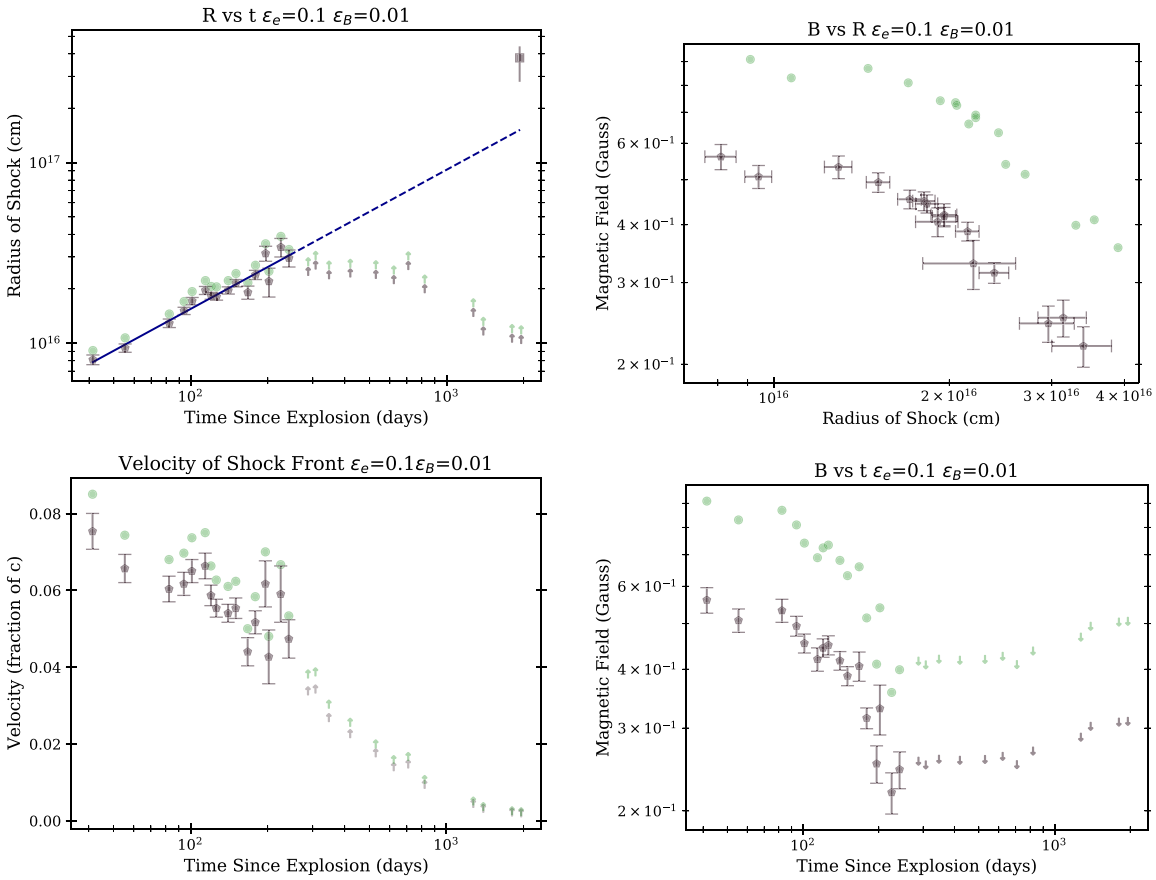

Figure 3. Physical parameters derived from $F_{\rm brk}$ and $\nu_{\rm brk}$ using our re-derived Equations (16) and (17) for different choices of microphysical parameters. Purple points correspond to the favored BPL model ($s=-1$, $\alpha_2=5/2$) with $\epsilon_B=0.01$, $\epsilon_e=0.1$. Green points are in equipartition ($\epsilon_B=\epsilon_e=1/3$) and have the same uncertainties as the purple points. Top-left panel: the blue line is the power-law fit $R\propto t^q$ of the purple points, where $q=0.77\pm0.04$. The dashed line is a continuation of this fit until the time of the VLBA measurement. The square point is our VLBA measurement of the radius ($3.8^{+0.6}_{-1.0}\times10^{17}$ cm) obtained at 1931 days since explosion. A re-fit incorporating this value agrees within uncertainties with the value inferred from modeling of VLA observations at <300 days since explosion.

velocity v_w, the CSM density is related to $\dot{M}$ as $\rho_{\rm CSM}=\frac{\dot{M}}{4\pi R^2 v_w}$. Combining Equations (17) and (22), the mass-loss rate at a radius probed by the forward shock thus satisfies the relation:

$$\frac{\dot{M}}{v_w}\left(\frac{1000\ \mathrm{km\ s^{-1}}}{10^{-4}M_\odot \mathrm{yr}^{-1}}\right) = 1.850\times10^{14}\left(\frac{\nu_{\rm brk}}{5\mathrm{GHz}}\right)^2\left(\frac{t}{\mathrm{days}}\right)^2(i+1)(c_1^2\epsilon_B q^2)^{-1}\times\left[\frac{(4.688\times10^{-23})\left(\frac{E_l}{\mathrm{erg}}\right)^{2(2-p)}\epsilon_B^2 c_5}{\sin\theta^{(5+2p)/2}\left(\frac{D}{\mathrm{Mpc}}\right)^2\epsilon_e^2\left(\frac{f}{0.5}\right)^2\left(\frac{F_{\rm brk}}{\mathrm{Jy}}\right)(p-2)^2c_6^3}\right]^{\frac{4}{(13+2p)}} \quad (24)$$

Similarly to $\rho_{\rm CSM}$, both n_e and $\dot{M}$ scale as $\propto\frac{i+1}{q^2}$. We emphasize that radio observations constrain the ratio $\dot{M}/v_w$ by providing $\rho_{\rm CSM}$ and that an independent estimate of v_w, from optical spectroscopy, for example, is needed to resolve for the model degeneracy. For CSM environments that deviate from a wind profile, Equation (24) provides an estimate of the *effective* mass-loss rate in units of v_w.

When substituting $q=7/8$, $p=3$, $i=1$, $E_l=mc^2$ and $\sin\theta\approx1$, the expression of Equation (24) can be compared to Equation (23) in Chevalier & Fransson (2006):

$$\frac{\dot{M}}{v_w}\left(\frac{1000\ \mathrm{km\ s^{-1}}}{10^{-4}M_\odot \mathrm{yr}^{-1}}\right) \overset{q=7/8}{=} 2.5\times10^{-5}\left(\frac{\nu_{\rm brk}}{5\mathrm{GHz}}\right)^2\left(\frac{t}{\mathrm{days}}\right)^2\epsilon_B^{-1}\times\left[\epsilon_B^2\left(\frac{D}{\mathrm{Mpc}}\right)^{-2}\left(\frac{F_{\rm brk}}{\mathrm{Jy}}\right)^{-1}\epsilon_e^{-2}\left(\frac{f}{0.5}\right)^{-2}\right]^{4/19}. \quad (25)$$

When we evaluate our Equation (23) instead at $q=1$ and $i=5/3$ and assume the material is fully ionized hydrogen (such that $\mu_e=1$), we recover Equation (16) of Ho et al. (2019; we note that they write their expression in terms of luminosity):

$$n_e \overset{i=5/3}{=} 1.02418\left(\frac{\nu_{\rm brk}}{5\mathrm{GHz}}\right)^4\left(\frac{t}{\mathrm{days}}\right)^2\epsilon_B^{-1}\times\left[\epsilon_B^{-3}\left(\frac{D}{\mathrm{Mpc}}\right)^{22}\epsilon_e^3\left(\frac{f}{0.5}\right)^3\left(\frac{F_{\rm brk}}{\mathrm{Jy}}\right)^{11}\right]^{-2/19}\mathrm{cm}^{-3}. \quad (26)$$

Equation (24) reduces to:

$$\frac{\dot{M}}{v_w}\left(\frac{1000\ \mathrm{km\ s^{-1}}}{10^{-4}M_\odot \mathrm{yr}^{-1}}\right) \overset{i=5/3}{=} 2.6\times10^{-5}\left(\frac{\nu_{\rm brk}}{5\mathrm{GHz}}\right)^2\left(\frac{t}{\mathrm{days}}\right)^2\epsilon_B^{-1} \times\left[\epsilon_B^2\left(\frac{D}{\mathrm{Mpc}}\right)^{-2}\left(\frac{F_{\rm brk}}{\mathrm{Jy}}\right)^{-1}\epsilon_e^{-2}\left(\frac{f}{0.5}\right)^{-2}\right]^{4/19}, \quad (27)$$

which is Equation (23) in Ho et al. (2019; in terms of flux and distance, rather than luminosity) once one accounts for the facts that: (i) Equation (23) in Ho et al. (2019) reports the wrong scaling for the filling factor f; and (ii) the reported normalization is also not correct ($\gtrsim$10 times larger than the correct value). See also footnote 4 of Yao et al. (2021). Our Equation (27) above gives the correct parameter scalings and normalization.

We conclude with considerations regarding the impact different values of i and q will have on pre-shock CSM density and mass-loss rates. In the radio SN literature, a diversity of parameterization choices map to values of i and q that we explore in Appendix C. It follows that inferred $\rho_{\rm CSM}$ values are *not* directly comparable to one another, even when the same microphysical parameters ϵ_e and ϵ_B are chosen. For example, using $i=5/3$ and $q=1$ (as in Ho et al. 2019) leads to a factor of $\frac{i+1}{q^2}=8/3\approx2.67$ in $\rho_{\rm CSM}$, and Chevalier & Fransson (2006) choose $i=1$ and $q=7/8$, which leads to $\frac{1+i}{q^2}\approx2.61$. Similarly, Equation (C2) employed by Matsuoka & Maeda (2020) is equivalent to $i=-1/2$ and $q=1$; this definition leads to $\frac{1+i}{q^2}=1/2$. Among a range of assumed i and q values in the literature (Appendix C), the ratio $\frac{1+i}{q^2}$ spans values 1/2–8/3, leading to reported values of $\rho_{\rm CSM}$ (as well as n_e and $\dot{M}$) that are *systematically different up to a factor* ≈5. We thus caution the reader regarding direct comparisons of $\dot{M}$ (or n_e or $\rho_{\rm CSM}$) values from independent works, even when the same shock microphysical parameters are used.

3.3. Radio SED Fitting

In this section we describe the fitting procedure used on the radio SEDs to extract the physical parameters of the emitting source based on the physics described in the previous sections. We model the radio SED produced by synchrotron emission described in Section 3.1 with a smoothed BPL of the form:

$$F_\nu = F_{\rm brk}\left[\left(\frac{\nu}{\nu_{\rm brk}}\right)^{\alpha_1/s}+\left(\frac{\nu}{\nu_{\rm brk}}\right)^{\alpha_2/s}\right]^s. \quad (28)$$

This functional form is widely used in the radio SN and nonjetted TDE literature (e.g., Soderberg et al. 2006c, 2006; Alexander et al. 2020 and references therein). The smoothing parameter s represents how abruptly the SED turns over from the "optically thick" slope (α_2) to the "optically thin" slope (α_1). For an SSA spectrum with $\nu_{\rm m}<\nu_{\rm sa}$, $\alpha_1=-(p-1)/2$, and we expect $\alpha_2=5/2$ (Equations (14) and (15)). Sharper transitions between slopes are associated with smaller s values. For the spectral regime of interest, $\nu_{\rm brk}$ can be identified as $\nu_{\rm sa}$. $F_{\rm brk}$ represents the peak flux density where the asymptotic power laws describing the optically thin and the optically thick spectrum meet (i.e., the $F_{\rm brk}$ parameter in Equation (28) is the break flux density that appears in the equations of the previous sections).

In general, $\nu_{\rm brk}\equiv\nu_{\rm brk}(t)$ and $F_{\rm brk}\equiv F_{\rm brk}(t)$. For a radio SN, the typical behavior is to observe a migration of $\nu_{\rm brk}$ to lower frequencies as time progresses, and the emitting region expands over a larger volume, leaving a broader range of higher frequencies optically thin to synchrotron radiation. We fit each SED without imposing a predefined temporal evolution of the parameters (in the SN literature, a power-law evolution of $\nu_{\rm brk}(t)$ and $F_{\rm brk}(t)$ is typically assumed; e.g., Soderberg et al. 2006) allowing us to reconstruct the actual density profile of the CSM created by the star before explosion, and hence the true mass-loss history of the progenitor. An example of this procedure on our data is represented in Figures 1 and 2, and the full SED evolution is Figure 10 in Appendix D.

The SED power-law slopes α_1 and α_2 are free parameters that can, in principle, take different values in each of the SEDs. Our fitting procedure provides the flexibility to jointly fit all of the available SEDs with common values of α_1 and α_2, along with the smoothing parameter s. At late times when the peak frequency has migrated below our observable frequency range, we fit the SED to a single-sided power law and include this information in a joint fit of the slopes. The information from single-sided SEDs provide lower and upper limits on physical parameters. Our fitting procedure thus does not assume any value for p; instead p can be derived from the best-fitting optically thin slope α_1. We use the BPL function of Equation (28) with `lmfit` and perform a least-squares minimization.

We point out that an important source of confusion in the radio SN literature is that the $F_{\rm brk}$ of Equations (16)–(23) is often incorrectly identified as the peak of the smoothed BPL flux density, as opposed to the intersection of the two asymptotic power laws. This is important because this implies that the true $F_{\rm brk}$ is underestimated by a factor of 2^s that propagates into all estimates of the physical parameters (see Equations (16)–(23)).

4. Modeling of the Radio SN 2004C and Physical Inferences

4.1. Radio SED Fitting of SN 2004C

The radio data of SN 2004C are reported in Table 3. We consider data acquired within date ranges $\delta t/t<0.025$ as part of the same SED. This procedure identifies 28 individual radio SEDs spanning the range $\delta t=41.41$–1938.22 days since explosion. We modeled each SED with the BPL function of Equation (28), and we jointly fit all of the SEDs with the same α_1, α_2 and s value, while allowing $F_{\rm brk}$ and $\nu_{\rm brk}$ to evolve from one SED to the other. We explored with our software four cases: (i) fixing both the thick slope $\alpha_2=5/2$ and $s=-1$ ("BPL1"), (ii) fixing only $s=-1$ ("BPL2"), (iii) fixing only the thick slope $\alpha_2=5/2$ ("BPL3"), and (iv) allowing both slopes and s vary ("BPL4").

We compare these models using an F-Test and report our results in Appendix B, Table 2. We adopt the standard p-value threshold of 5% to reject a given model, and χ^2 when the degrees of freedom are equal. We identify BPL1 ($s=-1$, $\alpha_2=5/2$) as the favored model by these statistics. The best-fitting model parameters for BPL1 are reported in Table 1. Figures 1, 2, and 10 show the best-fitting model and the data.

4.2. Inferred Physical Parameters of SN 2004C: p, R(t), and B(R)

We use the best-fitting parameters of Table 1, their uncertainties, and covariance information to estimate the physical parameters of the shock launched by SN 2004C and the circumstellar environment with which it interacts. First, the optically thin slope $\alpha_1 = -(p-1)/2$ implies a power-law index of the electron distribution $p = 2.92 \pm 0.06$, in-line with typical values inferred from SNe from the radio modeling of SNe $p \approx 3$ (e.g., Chevalier & Fransson 2006; Soderberg et al. 2006) and recently interpreted by Diesing & Caprioli (2021). Values of p show consistency among all of our fit models, falling within ∼0.1 of one another. Next, we estimate $R(t)$ and $B(t)$ using Equations (17) and (16), respectively. In our analysis, we adopt $i = 1$, and we infer $q = 0.77 \pm 0.04$ (Figure 3). We present our results for the case of equipartition ($\epsilon_e = 1/3$, $\epsilon_B = 1/3$) and for our fiducial case $\epsilon_e = 0.1$ and $\epsilon_B = 0.01$. We note that the radius and magnetic field scale as $R \propto \epsilon_e^{\frac{-1}{(13+2p)}} \epsilon_B^{\frac{1}{(13+2p)}}$ and $B \propto \epsilon_e^{\frac{-4}{(13+2p)}} \epsilon_B^{\frac{4}{(13+2p)}}$ and are thus minimally sensitive to specific assumptions of the shock microphysical parameters. Instead, $U(t) \propto \epsilon_e^{\frac{-11}{(13+2p)}} \epsilon_B^{\frac{11}{(13+2p)}-1}$, $\rho_{\rm CSM}(r) \propto \epsilon_e^{\frac{-6}{(13+2p)}} \epsilon_B^{\frac{6}{(13+2p)}-1}$, and $\dot{M}(r) \propto \epsilon_e^{\frac{-8}{(13+2p)}} \epsilon_B^{\frac{8}{(13+2p)}-1}$ are sensitive to the assumed ϵ_e and ϵ_B values and the assumption of equipartition conveniently provides solid lower limit on their values. Relatedly, radius scales as $R \propto D^{\frac{2(6+p)}{(13+2p)}}$ and mass loss as $\dot{M} \propto D^{\frac{-16}{(13+2p)}}$. Changes to the distance by a factor N moderately affect our results; for $p \approx 3$, R will change by a factor of $N^{0.9}$ and $\dot{M}$ by a factor of $N^{-0.8}$.

Figure 3 shows the evolution of the forward shock radius and shock velocity with time, implying mild deceleration of the shock as it interacts with material in the ambient medium. We find $R(t) \propto t^{0.77 \pm 0.04}$ over the distance range $(8.1 \pm 0.5) \times 10^{15}$– $(3.4 \pm 0.4) \times 10^{16}$ cm using observations acquired 41–1938 days since explosion. With the VLBA, we inferred $R = 3.8^{+0.6}_{-1.0} \times 10^{17}$ cm at 1931 days since explosion. The extrapolation of our best-fitting FS radius derived from VLA observations to the time of the VLBA observations is $R = (1.5 \pm 0.5) \times 10^{17}$ cm, which is consistent, but slightly lower, than the interferometry measurement at the 3σ level (Figure 3). We remark that this is an extrapolation over almost one order of magnitude in time. Including the VLBA measurement in the $R(t)$ fit, we find $q = 0.81 \pm 0.03$, which is consistent within uncertainties with the radius expansion rate that we infer at <242 days since explosion. The forward shock has an average shock velocity of $\approx 0.06\ c$ throughout the duration of our observations. For a power-law evolution of the shock radius with time, $R(t) \propto t^q$ the velocity is $v = q\frac{R}{t}$.

Instead of assuming a specific progenitor type and CSM density profile to compute q using the self-similar solutions by Chevalier (1982), we allow our code to be as agnostic and self-consistent as possible: we derive q by taking the slope of $R(t)$ (solid line in Figure 3). Other fitting methods that hold the SED slope constant for synchrotron emission or allow all BPL fit parameters to vary lead to reasonably similar values. Appendix C demonstrates the effect this has on derived physical quantities.

Figure 3 presents the inferred evolution of the magnetic field with shock radius $B(R)$: we find evidence for a clear change in the B evolution at $R_{br} \approx (1.96 \pm 0.10) \times 10^{16}$ cm, with a flat profile $B \propto R^{-0.13 \pm 0.08}$ at $R < R_{br}$ evolving to $B \propto R^{-1.10 \pm 0.07}$ at $R > R_{br}$. As a reference, SN shocks expanding in wind-like media where ϵ_e and ϵ_B are not time-varying quantities are expected to show $B \propto R^{-1}$ (Chevalier 1998). The location of this "break radius" is largely independent from the choice of microphysical parameters (Figure 3), due to the very mild dependence of R on ϵ_e and ϵ_B.

We end this section by noting that in the context of SSA radio spectra for which the data provide constraints on only one break frequency $\nu_{\rm sa}$, the parameters p, R, and B are the three

Table 1
SED Best-fitting Parameters for Our Baseline Model (BPL1), which Has an Assumed Smoothing Parameter and Optically Thick Slope $s = -1$, $\alpha_2 = 5/2$ and an Optically Thin Slope $\alpha_1 = -0.96 \pm 0.03$

SED Number	Days Since Explosion	$\nu_{\rm brk}$ (GHz)	$F_{\rm brk}$ (μJy)
0	39.65	N/A	N/A
1	41.41–42.36	9.8 ± 0.6	3710 ± 290
2	55.36	9.0 ± 0.5	4320 ± 300
3	82.40	10 ± 0.6	11400 ± 700
4	94.15	10 ± 0.4	14300 ± 700
5	101.21	9.3 ± 0.4	16000 ± 800
6	114.07	8.7 ± 0.5	18900 ± 1400
7	120.14	9.2 ± 0.4	18000 ± 800
8	126.08	9.3 ± 0.4	18400 ± 900
9	140.14	8.6 ± 0.3	18600 ± 800
10	150.18	8.0 ± 0.3	19400 ± 900
11	167.16	8.3 ± 0.6	16000 ± 800
12	178.98–179.04	6.4 ± 0.3	14800 ± 700
13	196.08	5.2 ± 0.5	16900 ± 1000
14	202.05	6.6 ± 0.9	13700 ± 1000
15	224.98–225.99	4.4 ± 0.5	14900 ± 1000
16	241.97—242.02	4.9 ± 0.4	13200 ± 800
17	284.84	$\leqslant 4.9$	$\geqslant 9400$
18	304.59	$\leqslant 4.9$	$\geqslant 11000$
19	343.67	$\leqslant 4.9$	$\geqslant 8500$
20	406.20–416.27	$\leqslant 4.9$	$\geqslant 9000$
21	523.47–523.90	$\leqslant 4.9$	$\geqslant 9000$
22	615.94	$\leqslant 4.9$	$\geqslant 7500$
23	701.60	$\leqslant 4.9$	$\geqslant 11000$
24	813.41	$\leqslant 4.9$	$\geqslant 5900$
25	1260.10	$\leqslant 4.9$	$\geqslant 3100$
26	1378.74	$\leqslant 4.9$	$\geqslant 2000$
27	1785.5	$\leqslant 4.9$	$\geqslant 1500$
28	1938.22	$\leqslant 4.9$	$\geqslant 1500$
29	2793.65	N/A	N/A

Note. "N/A" entries show SEDs containing only one point that could not be fit to a one-sided power law.

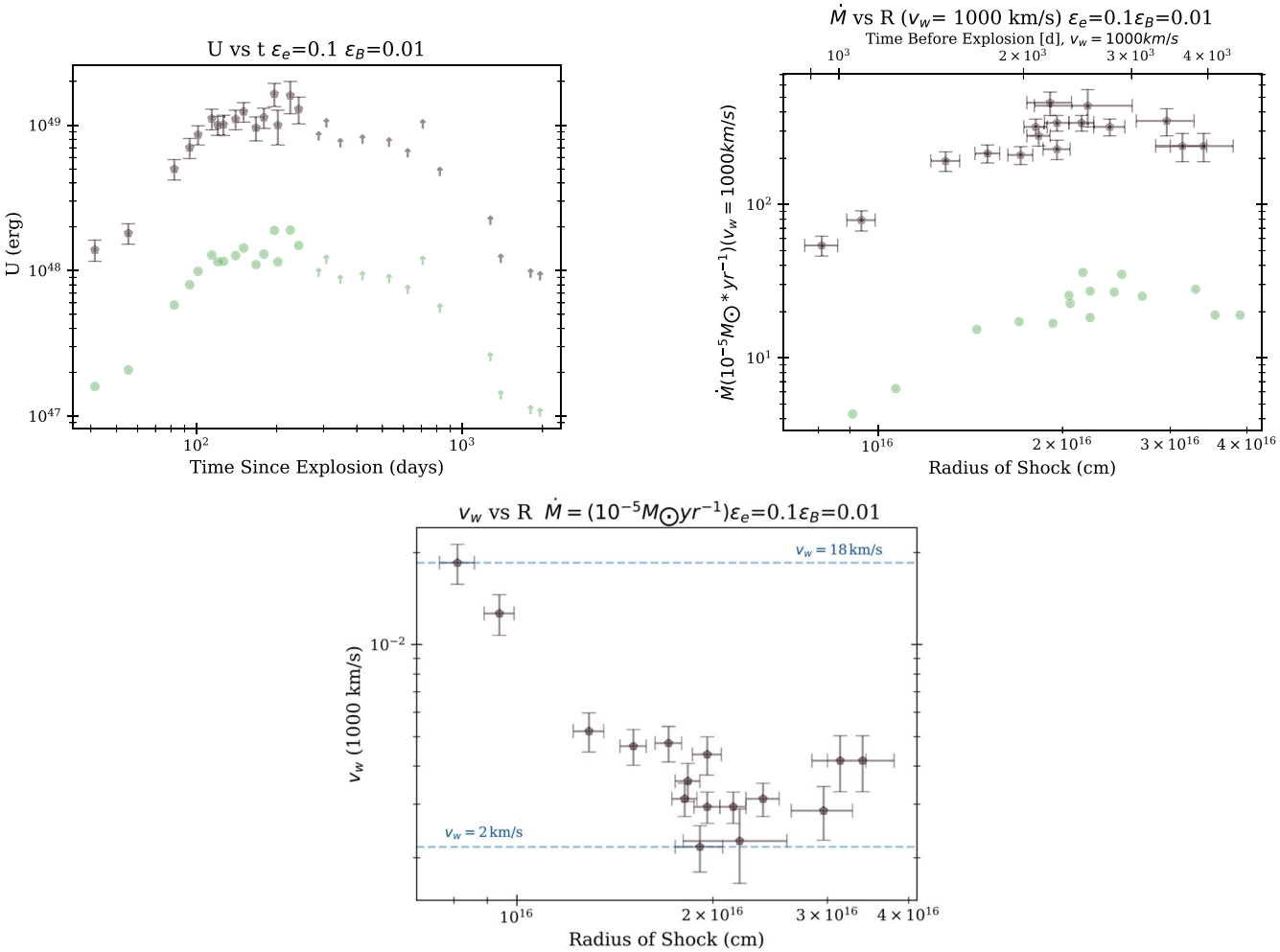

Figure 4. Physical parameters derived from $F_{\rm brk}$ and $\nu_{\rm brk}$ using our re-derived Equations (20) and (24) for different choices of microphysical parameters. Purple points correspond to the favored BPL model ($s = -1$, $\alpha_2 = 5/2$) with $\epsilon_B = 0.01$, $\epsilon_e = 0.1$. Green points are in equipartition ($\epsilon_B = \epsilon_e = 1/3$) and have the same uncertainties as the purple points. Top-left panel: blastwave energy U(t). Top-right panel: mass loss assuming a wind velocity of $v_w = 1000$ km s^{-1} as a function of forward shock radius, which probes the CSM as it expands. The top abscissa denotes the time before explosion this material left the progenitor assuming $v_w = 1000$ km s^{-1}. Bottom panel: progenitor wind velocity assuming $\dot{M} = 10^{-5}\ M_\odot$ yr^{-1} as a function of forward shock radius. Dashed lines: the lowest and highest wind velocities in the data set for this model and choice of microphysical parameters.

physical properties that can be independently constrained from the data. Any other parameters, such as those discussed in the next section, are derived from combinations of p, R, and B. Furthermore, the parameters sensitively depend on assumptions on the shock microphysical parameters. The implications of different definitions of the microphysical parameters on calculations of B, as well as the effect of the BPL model chosen, are elucidated in Appendices B and C.

4.3. Inferred Physical Parameters of SN 2004C: U, ρ_{CSM}, $\dot{M}$, and v_w

In our calculations of the physical parameters that follow, we utilize the value of q associated with the power-law slope of R versus t. We use Equations (20), (22), and (24) to calculate $U(t)$, $\rho_{\rm CSM}(R)$, and $\dot{M}(R)$. We find that in equipartition, the blastwave energy $U(t)$ increases with time from $(1.60 \pm 0.25) \times 10^{47}$ erg at 41 days since explosion to $(1.9 \pm 0.4)10^{48}$ erg at 242 days since explosion (Figure 4, green points). This behavior is consistent with the progressive conversion of ejecta kinetic energy into shock internal energy, as the stratified ejecta decelerates into the environment. These values are lower limits on the true shock internal energy because of the likely deviation from equipartition. However, as long as the shock microphysical parameters are constant with time, the ratio between the final and initial $U(t)$ is preserved, as is the temporal behavior of $U(t)$ or $\rho_{\rm CSM}(R)$.

With reference to Figure 5, our analysis highlights the presence of an internal region with roughly constant density extending to $R_{\rm br} \approx (1.96 \pm 0.10) \times 10^{16}$ cm, followed by a rapidly declining density profile with $\rho_{\rm CSM} \propto R^{-2.3\pm0.5}$ at $R > R_{\rm br}$. For a nominal ejection velocity of the CSM material by the progenitor of $v_w = 1000$ km s^{-1}, $R_{\rm br}$ corresponds to a look-back time of $\approx 10^{3.36}$ days (6.2 yr) prior to stellar collapse. Importantly, the $\rho_{\rm CSM}(R)$ profile that we derived from the radio observations violates the expectation from a single wind density profile, which predicts $\rho_{\rm CSM} \propto R^{-2}$. Our results point instead to the presence of a shell-like density structure $\sim 10^{16}$ cm from the explosion site of SN 2004C not unlike other stripped-envelope SNe such as SN 2004dk, ASASSN15no, SN 2017dio, and SN 2014C (Margutti et al. 2017; Benetti et al. 2018; Kuncarayakti et al. 2018; Balasubramanian et al. 2021; Stroh et al. 2021; Brethauer et al. 2022). Using early spectroscopic observations, Bruch et al. (2021) showed that >30% of hydrogen-rich SN progenitors experience large mass-loss events

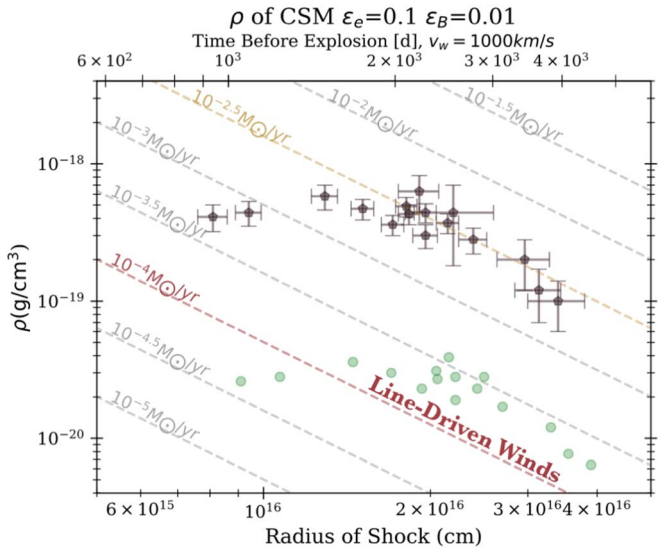

Figure 5. CSM density probed by the forward shock (upstream) as revealed by synchrotron emission at radio frequencies using our re-derived Equations (17) and (22). Purple points refer to values calculated using $\epsilon_e = 0.1$ and $\epsilon_B = 0.01$. Green points refer to values calculated in equipartition, $\epsilon_e = \epsilon_B = 1/3$; they will have the same uncertainties as the purple points. Diagonal lines: comparison to constant mass loss assuming $v_w = 1000$ km s^{-1}. The mass-loss rate of SN 2004C is much greater than can be explained by line-driven winds (red dashed line; $\dot{M} = 10^{-4}\,M_\odot$ yr^{-1}) even at extreme luminosities $L = 10^6\,L_\odot$. The yellow dashed line denoting $\dot{M} = 10^{-2.5}\,M_\odot$ yr^{-1} is to assist the reader's estimate of the slope. Top abscissa: time before explosion material was deposited in the CSM, assuming $v_w = 1000$ km s^{-1} and free expansion.

shortly prior to explosion. Interestingly, the phenomenology of mass lost to the environment in the last moments of evolution extends all the way to SLSNe (i.e., iPTF15esb, iPTF16bad, and SN 2017ens), which presumably have different progenitors (Yan et al. 2017; Chen et al. 2018).

Radio observations constrain the ratio $\rho_{\rm CSM} \propto \dot{M}/v_w$ but do not independently constrain $\dot{M}$ and/or v_w. It follows that the shell-like density profile around SN 2004C can be the result of a time-varying mass-loss rate $\dot{M}(t)$ or a time-varying progenitor wind $v_w(t)$, or both. Figure 4 (upper panel) shows the $\dot{M}$ profile as a function of radius and look-back time, if the progenitor had a roughly constant $v_w \sim 1000$ km s^{-1}. Taken at face value, these results imply that in this case the very last phases of evolution of the progenitor at $t < 10^{3.36}$ days (6.2 yr) have been characterized by a rapidly decreasing $\dot{M}$ with time, with $\dot{M}$ reaching a peak value of $\dot{M} \approx (460 \pm 80) \times 10^{-5}\,M_\odot$ yr^{-1} (for $\epsilon_e = 0.1$ and $\epsilon_B = 0.01$). We note that $\frac{\dot{M}}{v_w} \propto e_B^{\frac{8}{(13+2p)}-1} e_e^{\frac{-8}{(13+2p)}}$ (Equation (24)), so assume equipartition versus the fiducial values of ϵ_e and ϵ_B can reduce the mass loss inferred by nearly a factor of ~3 (Figure 4). We report our results in Tables 4 and 5 in units of $10^{-5}\,M_\odot$ yr^{-1} and $v_w = 1000$ km s^{-1} as these values are representative of WR stars in our galaxy ($\dot{M} = 10^{-5.6} - 10^{-4.4}$ $M_\odot$ yr^{-1} and $v_w < 6000$ km s^{-1}; Crowther 2007).

For the complementary case of a constant $\dot{M} \approx 10^{-5}\,M_\odot$ yr^{-1} (Figure 4), the observed density profile would instead imply a significant change in the wind velocity in the last few thousands of years preceding core collapse, with a rapid increase of one of magnitude in the final ~3000 yr (from 2–18 km s^{-1} for our assumed $\dot{M}$ unit value). These winds' velocities are clearly not consistent with a compact, single WR star.

In reality, neither of these two limiting cases might apply. The shell-like structure might be the result of a "wind–wind interaction," where faster, lighter winds interact with mass lost to the environment through slower winds of the preceding phase of stellar evolution, for example, during the red supergiant (RSG) → WR transition (Heger et al. 2003; van Loon et al. 2005; Dwarkadas et al. 2010; Mauron & Josselin 2011). We explore the "wind–wind interaction" scenario and additional explanations in the following section.

5. Mass-loss Discussion

The major result of modeling our radio observations is a radial profile in $\rho_{\rm CSM}(R)$ that is robust against the choice of SED fit model (Figures 5 and 9). Most importantly, this profile reveals a structure in the CSM that is flat ($\rho \propto R^{-0.03\pm0.22}$) out to $(1.96 \pm 0.10) \times 10^{16}$ cm, followed by an immediate, steep decline of $\rho \propto R^{-2.3\pm0.5}$.

The maximum mass-loss rate that can be supported by line-driven winds depends on metallicity Z and the luminosity L of the progenitor star as follows (e.g., Gayley 1995; Smith & Owocki 2006):

$$\dot{M}_{\rm max,lines} = 7 \times 10^{-3} Z L_6 M_\odot {\rm yr}^{-1}, \quad (29)$$

where $L_6 \equiv 10^6\,L_\odot$. For solar composition, the hydrogen, helium, and metal fractions by mass are $X_\odot = 0.7381$, $Y_\odot = 0.2485$, and $Z_\odot = 0.0134$, respectively (Asplund et al. 2009). NGC 3683, the host galaxy of SN 2004C, has approximately solar metallicity of about $12 + [{\rm O/H}] = 8.74$ dex (Kelly & Kirshner 2012).[16] For the most luminous stellar progenitors with $L_6 \sim 1$ at solar metallicity, Equation (29) implies $\dot{M}_{\rm max,lines} \approx 7 \times 10^{-5}$ $M_\odot$ yr^{-1}, but SN 2004C shows a maximum mass-loss rate of $(460 \pm 80) \times 10^{-5}\,M_\odot$ yr^{-1} (assuming $v_w = 1000$ km s^{-1}, $\epsilon_B = 0.01$, and $\epsilon_e = 0.1$), two orders of magnitude greater than the limit of single line-driven winds. We conclude that a single fast wind ($v_w = 1000$ km s^{-1}) from a compact progenitor cannot sustain the large mass-loss rates inferred for SN 2004C.

We now compare SN 2004C to mass-loss rates observed in massive stars. The densities measured for SN 2004C overlap in the $\dot{M}$ versus v_w phase space with RSG and luminous blue variable (LBV) progenitors, because RSGs have significantly slower winds, and LBVs are not powered by line-driven winds (Figure 6). However, both cases expect copious H in the ejecta, which was *not* observed for SN 2004C (Shivvers et al. 2017). Assuming a WR wind speed of 1000 km s^{-1}, the inner density profile of SN 2004C corresponds to a mass-loss rate of $(54 \pm 8) \times 10^{-5}\,M_\odot$ yr^{-1} at radius $R = (8.1 \pm 0.5) \times 10^{15}$ cm (with $\epsilon_B = 0.01$ and $\epsilon_e = 0.1$; Equation (24), Figure 4). WRs typically span a range of mass-loss rates $\dot{M} \approx 10^{-5.6} - 10^{-4.4}$ $M_\odot$ yr^{-1}, which is significantly lower than observed in SN 2004C for the same wind velocity (Crowther 2007, compare WR box to SN 2004C shell in Figure 6). Similarly, the region of SN 2004C that overlaps with the parameter space partitioned to RSGs can be ruled out, as RSGs are H-rich, and we did not see H in the spectra of SN 2004C (Shivvers et al. 2017). This comparison to known stellar mass-loss rates strengthens our previous conclusion that a single line-driven wind cannot produce the CSM material surrounding SN 2004C; and instead we must invoke slower winds or multiple line-driven winds (Figure 6).

[16] At the explosion site, there is evidence for super-solar metallicity (Dittman, private communication).

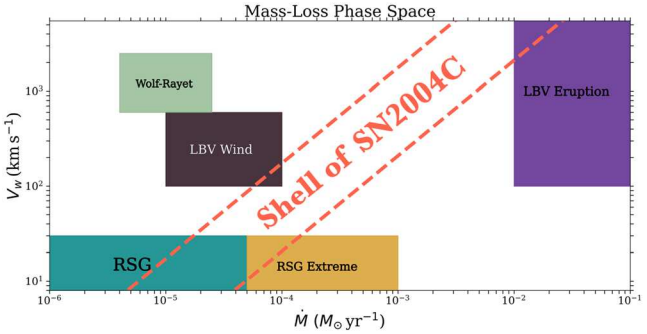

Figure 6. Wind velocity vs. mass-loss rate phase space (see Section 5 for full discussion). Blue shaded region: mass-loss rates of main-sequence stars and subgiants. Rates are taken from Seaquist et al. (1993). Light green shaded region: mass-loss rates of Wolf–Rayet stars from Crowther (2007). Brown shaded region: mass-loss rates from LBV continuum winds (Smith 2014; Terreran et al. 2019, and references therein). Teal shaded region: wind speeds and mass-loss rates of red supergiant stars (RSGs; Seaquist et al. 1993). Gold shaded region: extreme winds possible in RSGs (de Jager et al. 1988; Marshall et al. 2004; van Loon et al. 2005). Purple shaded region: observed mass losses of LBV eruptions (Smith & Owocki 2006). Orange diagonal-dashed lines: the parameter space constrained by our observations of $\dot{M}/v_w$ in SN 2004C. Note that although RSG winds fall within the realm of possibility, they have not been identified as SN Type IIb progenitors.

As an alternative, continuum-driven winds can power larger mass-loss rates than line-driven winds due to their dependence on the electron scattering cross section rather than the cross sections of metals in the stellar atmosphere. In principle, this implies that continuum-driven winds are not as sensitive to metallicity. However, even if continuum-driven winds could manage to supply a constant mass-loss rate at the appropriate magnitude, we find the single-wind mechanism as a whole is in tension with the observed CSM density profile surrounding SN 2004C. A single wind (line- or continuum-driven) with a constant mass-loss rate would create an environment density that scales with $\rho \propto R^{-2}$, rather than the measured $\rho \propto R^{-0.03\pm0.22}$ that transitions to $\rho \propto R^{-2.3\pm0.5}$ (Figure 5).

Instead, the density profile that we infer from radio observations requires us to consider more exotic forms of mass loss or wind–wind interaction scenarios. We investigate the possibility the CSM could have been sculpted by the interaction of multiple winds or time-varying winds in Section 5.1. We explore the possibility that this shell of material was ejected by a single event (i.e., a shell-ejection scenario) in Section 5.2.

5.1. Wind–Wind Interaction and Time-varying Continuum Winds

Wind–wind interaction can occur in the circumstellar medium where a faster-moving wind encounters a slower-moving wind launched by the star at an earlier date. For reference, free expansion of a wind would produce a density profile $\rho \propto R^{-2}$, which is not too dissimilar from the outer shell density profile we observe in SN 2004C, where $\rho \propto R^{-2.3\pm0.5}$ (Figure 5). In the SN literature, wind–wind interaction models have been invoked to explain the "anomalous" density profiles found around SN 1996cr (Dwarkadas et al. 2010) and SN 2001em (Chugai & Chevalier 2006). Chugai & Chevalier (2006) speculated that the shell of material around SN 2001em resulted from a combination of late-stage mass transfer in a binary system followed by an RSG → WR transition. In this instance, both stages could could have polluted the environment and subsequently swept up the CSM as winds accelerated, then pushed the shell out to a radius of $\sim 10^{16}$ cm. In the case of a single star, the transition to a compact WR phase (which is associated with a faster wind) is expected to take place ≈0.5–1 Myr before explosion, much earlier than the approximate shell age of 1000 yr in SN 2004C (Dwarkadas et al. 2010; Margutti et al. 2017). However, for some binaries, the envelope removal of the primary star by binary interaction can happen much closer to the epoch of core collapse, as it was proposed for SN 2014C (Milisavljevic et al. 2015; Margutti et al. 2017). A similar connection between progenitor envelope and binary-induced mass loss was also proposed for Type IIb SNe by Maeda et al. (2015). It is possible that SN 2004C resembles this scenario, requiring a binary system and a shorter WR phase than what single-star evolution allows. In this case, faster winds sculpt slower-moving winds in the CSM, and the star consequently explodes as a stripped-envelope SN.

Radio observations of the type IIb SN2001ig showed an undulating light curve, for which Ryder et al. (2004) and Ryder et al. (2006) explored the implications of a binary companion to a WR star in the case of SN 2001ig. These studies posit that a hot, extended companion may sculpt the CSM around a WR star, and a sufficiently eccentric orbit may create a "pinwheel" pattern in the CSM. When viewed edge-on, thick portions of the pinwheel can resemble a circumstellar shell (however, Soderberg et al. 2006 points out that this would require the same geometry and viewing angle as SN2001ig). While the two SNe display fluctuations in their light curves at 4.9 and 8.5 GHz (Figure 2), those in SN 2004C occur at later phases and at a significantly higher luminosity (the distance to SN 2004C is 35.9 Mpc, while SN 2001ig is located 11.5 Mpc away; Ryder et al. 2004). While the pinwheel explanation lacks support from our analysis, we do not rule out binary interaction as an underlying cause of the CSM structure.

As 1000 yr is an upper limit on the age of the shell, wind speeds less than 1000 km s^{-1} would produce shells younger than 1000 yr. In particular, if the wind speed was 10 km s^{-1}, the shell would have been produced only a few years before collapse, requiring a very different pre-explosion history and an expulsion mechanism triggered much closer to the time of collapse. We limit our conclusions to what we may speculate with confidence regarding the shape of the density profile.

Irrespective of the physical origin of the CSM shell, sustained mass loss in the final decades before explosion can significantly modify the stellar progenitor structure at the time of explosion. It is thus instructive to review our current knowledge of stellar progenitors of Type IIb SNe. Based on pre-explosion imaging with HST (Smartt 2015), the prominence of the cooling-envelope phase in the optical light curve (e.g., Arcavi et al. 2011), and the dynamic of the fastest outflows launched by the explosions as constrained by radio observations (Soderberg et al. 2012),[17] the stellar progenitors of Type IIb SNe show diversity in their structure, from extended yellow hypergiants like the recent SN 2016gkg (Kilpatrick et al. 2017; Piro et al. 2017; Tartaglia et al. 2017; Orellana et al. 2018; Sravan et al. 2018; Kilpatrick et al. 2022) to more compact progenitors with $R_{\rm star} < 50\,R_\odot$, as in the case of Type IIb SN 2008ax (e.g., Crockett et al. 2008; Roming et al. 2009; Groh et al. 2013;

[17] Note however that the progenitor star of SN 2011dh was likely extended, in spite of having launched an outflow with properties similar to those of the more compact Ib-Ic SN progenitors (see Folatelli et al. 2014, and references therein).

Folatelli et al. 2015; Yoon et al. 2017). Based on the current constraints on masses and radii of Type IIb progenitors (compiled from Sravan et al. 2020; Gilkis & Arcavi 2022 and references in both), the inferred escape velocities lie in the range 45–300 $\mathrm{km\,s^{-1}}$, which maps into typical stellar wind velocities of 135–900 $\mathrm{km\,s^{-1}}$ (order of magnitude estimate). We note that the current sample of Type IIb SNe with detected progenitors is biased toward the more extended stars, and that compact stars that are more difficult to detect are associated with faster winds. In this sense, the estimates above should be viewed as a likely lower limit on the true wind velocity of SN 2004C just before explosion. We thus conclude that for SN 2004C, $v_w \gtrsim 100$ $\mathrm{km\,s^{-1}}$ at the time of the explosion, which implies large mass-loss rates $\dot{M} \gtrsim 10^{-4}\,M_\odot\ \mathrm{yr^{-1}}$.

5.2. Shell-ejection Scenarios

Unlike steady winds, shell-ejection scenarios mark an abrupt, sudden, and violent expulsion of mass from the progenitor, often triggered by an internal deposition of energy (Quataert & Shiode 2012; Woosley & Heger 2015; Woosley 2017; Leung et al. 2019; Leung & Fuller 2020; Wu & Fuller 2021). In SN 2004C, we observe a structure in the CSM between $(8.1 \pm 0.5) \times 10^{15}$ cm and $(3.4 \pm 0.4) \times 10^{16}$ cm. Assuming a constant wind speed of 1000 $\mathrm{km\,s^{-1}}$, our model suggests this structure was produced over the course of $10^{2.97}$ days (2.6 yr)–$10^{3.59}$ days (10.8 yr) before core collapse (Figure 5). Therefore, we find evidence pointing to a shift in the behavior of the progenitor star in the final 10^{-5}%–0.01% of its lifetime.

Traces of violent, substantial outbursts depositing material $\sim 10^{16}$ cm from the star at the time of explosion have been reported across multiple SN types. Hydrogen-poor SNe Types Ib/c, IIb (such as SN 2004C), and even SLSNe-I show evidence of CSM shells at this distance as we continue to monitor these events at late times with radio observations (Yan et al. 2017; Benetti et al. 2018; Kuncarayakti et al. 2018; Lunnan et al. 2018; Mauerhan et al. 2018; Gomez et al. 2019; Kundu et al. 2019; Prentice et al. 2020; Jacobson-Galán et al. 2021; Dong et al. 2021; Gutiérrez et al. 2021; Jin et al. 2021; Maeda et al. 2021; Stroh et al. 2021; Brethauer et al. 2022; SN 2019yvr; K. Auchettl 2022, in preparation; and the sampled population in Hosseinzadeh et al. 2022).

An extreme case of continuum-driven winds is an LBV outburst (Humphreys et al. 2017, 2019). These hot, blue stars quickly ionize stellar material, creating a large population of free electrons. In turn, the electrons serve as cross sections for radiative absorption and form metallicity-independent continuum-driven winds (Smith 2014). Outbursts become progressively more extreme the closer a star gets to its Eddington limit, consequently providing a spectrum of mass-loss events and outbursts. Such outbursts have been posited to source quasiperiodic mass loss observed in SNe at radio wavelengths (e.g., Kotak & Vink 2006). For example, η Car's Great Eruption in the nineteenth century involved a loss of about 12–20 $M_\odot$ of stellar material. The majority of this material was lost over 5 yr, but a lower limit of about $\dot{M} = 0.5\ \mathrm{yr^{-1}}$ is estimated for the average over the ≈20 yr duration of the eruption (Smith & Owocki 2006). Another example is the 1600 eruption of P-Cygni, wherein 0.1 $M_\odot$ was lost, implying a rate of $\dot{M} = 10^{-2}\,M_\odot\ \mathrm{yr^{-1}}$ due to continuum winds (Owocki et al. 2004; Smith & Owocki 2006). These specific ejected mass and mass-loss rates are significantly larger than the $M \approx 0.021\ M_\odot$ CSM shell observed in SN 2004C (Figures 5 and 6). Very early spectra of the Type IIb SN 2013cu revealed the presence of dense CSM confined within 10^{13} cm of the progenitor (Gal-Yam et al. 2014). While an LBV progenitor was suggested by quantitative modeling of these early-time spectra (Groh 2014) and of the transitional Type Ibn/IIb SN 2018gjx (Prentice et al. 2020), SN 2004C, shows a clear difference from the historical LBV eruptions because its progenitor underwent core collapse shortly after shell ejection. Furthermore, mass-loss rates of $>10^{-3}\,M_\odot$ are rare and have not been observed in living LBVs within the last few decades (Davidson 2020). In the following, we explore shell-ejection mechanisms that are tied to the requirement of imminent core collapse.

In the case of "pulsational pair-instability" SNe (PPISNe), stars with He cores $M > 30\,M_\odot$ can undergo electron-positron pair production, removing pressure in their cores that would otherwise support the star against the crush of gravity. Consequential pulses rippling through the star can launch enormous amounts of mass at the stellar surface, or even the H envelope itself (0.3 to several $M_\odot$; Woosley 2017). Because PPISNe exhibit multiple eruptions of unstable mass loss that mimic SNe, there is no way to know for certain if an explosion is a PPISN without observing a second eruption (Woosley 2017). Additionally, pre-SN core masses large enough for PPISNe require large zero-age main-sequence (ZAMS) masses (e.g., 70–260 $M_\odot$), greatly favoring low-metallicity (subsolar) environments (Woosley 2017). Because the host galaxy of SN 2004C is about solar metallicity (with possibly a higher metallicity concentration at the site of the explosion; Dittman, private communication), we rule out the PPISN mechanism as an underlying explanation to our observations.

Another mechanism we consider is gravitational waves, or wave heating. Proposed by Quataert & Shiode (2012), hydrodynamic waves during late-stage nuclear burning can excite violent convection. At the onset of core carbon burning, neutrino cooling is unable to fully dissipate the generated energy and as a result, the extreme convection launches internal gravitational waves with energies $\sim 10^7\,L_\odot$ (Fuller & Ro 2018). Barring large amounts of nonlinear wave breaking and damping throughout the body of the star (explored thoroughly in Wu & Fuller 2021 and Fuller & Ro 2018), the wave energy that survives to the surface can unbind mass, accelerate it above the escape velocity, and result in observable mass loss.

Fuller & Ro (2018) explored the wave heating mechanism in stripped and partially stripped progenitors at solar metallicity with 1D MESA models. Their models result in Type Ib/c and IIb SNe and place CSM material too nearby (within 6×10^{14} cm) to apply to SN 2004C. Similarly, Wu & Fuller (2021) conclude that stars of $M < 30\,M_\odot$ could exhibit gravitational-wave-driven mass-loss outbursts in the years to decades before explosion, which is too late in the life of a star to be relevant for SN 2004C. Specifically, their H-poor models with $M_{\mathrm{ZAMS}} = 36$–$40\,M_\odot$ end their lives as $M \sim 15\,M_\odot$ WR stars. In this case, the energy generated by gravitational waves was sufficient to eject $10^{-2}\,M_\odot$, but the ejected mass only reached $r \sim 10^{14}$ cm before core collapse, significantly smaller than the inner radius of $(8.1 \pm 0.5) \times 10^{15}$ we observe in SN 2004C. Their model with the most distant CSM material ($r \sim 10^{15}$ cm) was an $11\,M_\odot$ yellow supergiant progenitor, which lost $1\,M_\odot$ over the 10 yr prior to core collapse. $1\,M_\odot$ is much larger than the 0.021 $M_\odot$ observed in SN 2004C between $(8.1 \pm 0.5) \times 10^{15}$ and $(3.4 \pm 0.4) \times 10^{16}$ cm. Leung et al. (2021b) also predicted mass-loss rates of $10^{-5} - 10^{-3}\,M_\odot \mathrm{yr^{-1}}$

out to $10^{12}-10^{14}$ cm in stripped progenitors $M_{\rm ZAMS}=(20–90)\,M_{\odot}$ and metallicities $Z=(0.002–0.02)$. These mass-loss rates are both too low, and the resulting CSM shells are too close-in to reproduce the situation of SN 2004C. At the time of writing, current wave-driven models do not match the time-scales and distances observed in SN 2004C; and it is unclear if future simulations of wave-driven mass loss could reproduce the measurements of SN 2004C. We conclude that if related to wave-driven instabilities, the phenomenology that we observe in SN 2004C requires this mechanism to be active earlier than nuclear burning stages.

As a result of pre-explosion imaging coupled with modeled interactions, binary star systems are one of the favored progenitor systems of SNe IIb (Fox et al. 2014; Yoon et al. 2017; Zapartas et al. 2017; Ryder et al. 2018; Sravan et al. 2019). The amount of stripping the primary star undergoes from the secondary companion strongly depends on the initial masses of the system, the initial separation of the two bodies, and their metallicities (Smith & Arnett 2014; Yoon et al. 2017). It is believed that about two-thirds of massive stars are members of binary systems that interact before stellar death, and both early and late Case B mass transfer (when the donor star is evolving into an RSG) can induce primary stars to become blue hypergiants, yellow hypergiants, and RSGs—all progenitors of SNe Type IIb (Fox et al. 2014; Smith & Arnett 2014; Yoon et al. 2017; Ryder et al. 2018). We find that we cannot rule out binary stripping and its possible effects on mass-loss winds throughout the lifetime of SN 2004C, because binary interaction is capable of ejecting the entire hydrogen envelope of a star over a variety of timescales (Fox et al. 2014; Yoon et al. 2017; Ryder et al. 2018).

6. Conclusions

In this paper, we began with the synchrotron derivation of the radio emission from an SN shock by Chevalier (1998) and present here the expressions for the post-shock magnetic field B, forward shock wave radius R, shock internal energy U, circumstellar density $\rho_{\rm CSM}$, and associated mass-loss rate $\dot{M}$, generalized for any value of the power-law index of the electron density distribution, p. As part of our generalized formalism, we reviewed the different definitions of the shock microphysical parameters ϵ_e and ϵ_B that are used in the radio SN literature, and we show in detail how hidden assumptions can lead to systematically different inferences of the shock and environment parameters, even when the same microphysical parameters values are adopted. These discrepancies are summarized and quantified in Appendix C. We applied our generalized formalism of Equations (16)—(24) to a collection of 7.7 yr of multifrequency radio data of SN 2004C, and we showed how this formalism leads to inferences on the forward shock dynamics that are in agreement with our direct VLBI measurements. Our modeling revealed the presence of a dense shell of CSM material containing a mass of 0.021 $M_{\odot}$ at a distance of about 10^{16} cm from the explosion. Our major results can be summarized as follows:

1. The shock microphysical parameters ϵ_e and ϵ_B have been defined in different ways in the radio SN literature. In this work, we quantitatively show the impact of the most common definitions of these parameters on the inferred shock and environment parameters; and we present a parameterization that will enable a direct comparison of the inferences from different works in the literature. We emphasize that in the specific case of the mass-loss rates, different, typically hidden, definitions lead to $\dot{M}$ values that can differ up to a factor of ∼5—even for the same choice of value for the shock microphysical parameters. These are compared in Appendix C.
2. Our radio modeling reveals a density profile with a flat structure in the CSM ($\rho\propto R^{-0.03\pm0.22}$) out to $(1.96\pm0.10)\times10^{16}$ cm, and an abrupt transition to $\rho\propto R^{-2.3\pm0.5}$ at larger radii. The most important result from the modeling of our radio observations is that a radial profile density $\rho_{\rm CSM}(R)$ in SN 2004C that exists independently of the fitting model (Figures 5 and 9).
3. If the 0.021 $M_{\odot}$ of CSM material around SN 2004C was created by a shell-ejection event, the implied ejection epoch is 128–2.5 yr prior to explosion for ejection velocities between 20 and 1000 km s^{-1}.
4. Of the mass-loss mechanisms we discuss in Section 5, we assert a single, line-driven wind with constant speed and mass-loss rate *could not* have sculpted the structure observed in the CSM of SN 2004C (Figure 6). Instead, multiple line-driven winds, a single time-varying wind, or a time-varying $\dot{M}$ could be responsible. We cannot rule out binary interaction as the underlying cause. While the extreme limits of gravitational waves/wave heating and LBV mass-loss rates marginally overlap with the uncertainties of our calculated rates, current models predict material either too close to the star or released too slowly.

The connection between the shell characteristics, mass-loss mechanism, and timing of mass-loss events events highly suggests a fundamental aspect of stellar evolution in evolved massive stars at work. Other SNe across different explosion types exhibit similarly substantial overdensities in their environments at $r\sim10^{16}$ cm from their explosion site (Margutti et al. 2017; Yan et al. 2017; Benetti et al. 2018; Chen et al. 2018; Kuncarayakti et al. 2018; Leung et al. 2021a; Jacobson-Galán et al. 2021, 2022; Hosseinzadeh et al. 2022; Stroh et al. 2021), possibly suggesting a shared mechanism. By observing changes in radio emission from the SN shock wave to probe the CSM density, we gather observational evidence that a rich and complex mass-loss history exists in stars, implying episodic mass loss in their final moments while they are on the verge of collapse. Consequently, the inability to conclusively point to any particular mechanism as the underlying cause highlights the need to model the final moments of late-stage core burning in H-poor progenitors.

L.D. heartily thanks Avni Coda for her contribution to all data visualization and gratefully acknowledges the help of tablesgenerator.com for importing .csv files as LaTeX tables with minimal headache. The authors would like to thank the anonymous referee for constructive, thoughtful, and insightful comments. L.D. is grateful for the partial financial support of the IDEAS Fellowship, a research traineeship program funded by the National Science Foundation under grant DGE-1450006. The National Radio Astronomy Observatory is a facility of the National Science Foundation operated under cooperative agreement by Associated Universities, Inc. The Margutti team at UC Berkeley and Northwestern is supported in part by the National Science Foundation under grant Nos. AST-1909796 and AST-1944985, by the Heising-Simons Foundation under grant # 2018-0911. R.M. is a CIFAR Azrieli Global Scholar in the Gravity & the Extreme Universe

Program 2019, and a Sloan Fellow in Physics, 2019. W.J.-G. is supported by the National Science Foundation Graduate Research Fellowship Program under grant No. DGE-1842165. W.J.-G. acknowledges support through NASA grants in support of Hubble Space Telescope programs GO-16075 and 16500. D.M. acknowledges NSF support from grants PHY-1914448 and AST-2037297. Parts of this research was supported by the Australian Research Council Centre of Excellence for All Sky Astrophysics in 3 Dimensions (ASTRO 3D), through project No. CE170100013. Research at York University was supported by the Natural Sciences and Engineering Research Council of Canada.

Software: lmfit (Newville et al. 2014), SNID (Blondin & Tonry 2007), ParselTongue (Kettenis et al. 2006).

Appendix A
Synchrotron Constants

We report the constants found in Pacholczyk (1970), which are used throughout Section 3. In the following, p is the power-law evolution of the accelerated electrons distributed in electron Lorentz factor γ_e, with minimum Lorentz factor γ_m: $dN(\gamma_e)/d\gamma_e = K_0\gamma_e^{-p}$ for $\gamma_e \geqslant \gamma_m$. N is the number of electrons per unit volume, and K_0 is the normalization. Other constants in the following equations include the charge of the electron e, the mass of an electron m_e, the speed of light c, and the Gamma function $\Gamma(p)$. All constants are in c.g.s. units.

$$c_1 = 6.27 \times 10^{18} \tag{A1}$$

$$c_5 = \frac{\sqrt{3}}{16\pi}\frac{e^3}{m_e c^2}\frac{p+\frac{7}{3}}{(p+1)}\Gamma\left(\frac{3p-1}{12}\right)\Gamma\left(\frac{3p+7}{12}\right) \tag{A2}$$

$$c_6 = \sqrt{3}\frac{\pi}{72}em_e^5c^{10}(p+\frac{10}{3})\Gamma\left(\frac{3p+2}{12}\right)\Gamma\left(\frac{3p+10}{12}\right) \tag{A3}$$

Appendix B
Model Comparison

Table 2 is a statistical comparison of the performance of different SED models. We first employ the F-Test, which begins by calculating the F-statistic, generally expressed as:

$$F = \frac{(\chi_1^2/\mathrm{dof_1})}{(\chi_2^2/\mathrm{dof_2})}. \tag{B1}$$

Model 1 has a larger number of degrees of freedom (dof) and fewer free parameters (M_{params}). Our null hypothesis (H_0) is

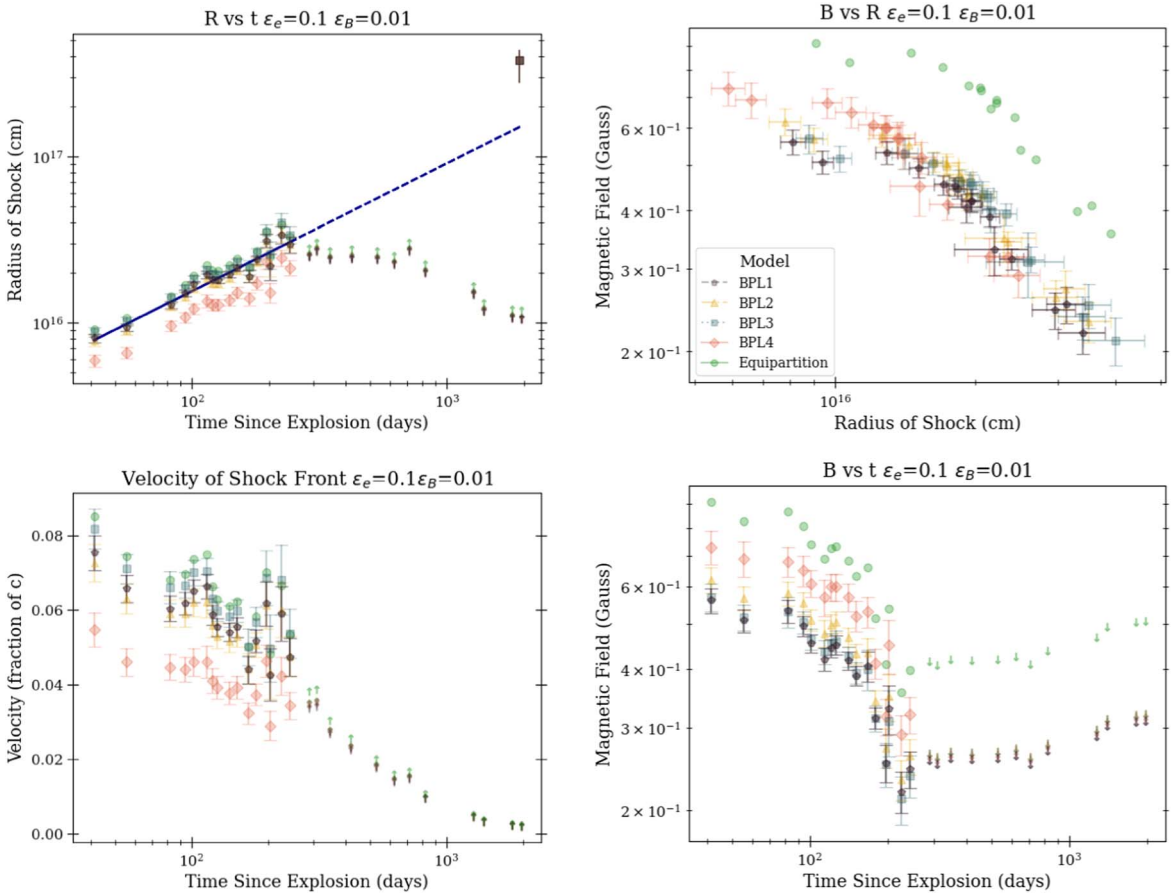

Figure 7. The same as Figure 3, but with all models compared in Section 3.3 and Appendix B. Note that the normalization differs between models, but the overall evolution remains the same. Purple pentagons: favored model where smoothing parameter is fixed at $s = -1$ and the slope $\alpha_2 = 5/2$ ("BPL1"). Yellow triangles: only smoothing parameter is fixed $s = -1$ ("BPL2"). Blue squares: only slope is fixed $\alpha_2 = 5/2$ ("BPL3"). Pink diamonds: All slopes and s are free to vary ("BPL 4"). Green points: BPL1 in equipartition ($\epsilon_B = \epsilon_e = 1/3$). Top-left panel: the blue line is the power-law fit $R \propto t^q$, where $q = 0.77 \pm 0.04$ and appears in our generalized formulae as the variable q.

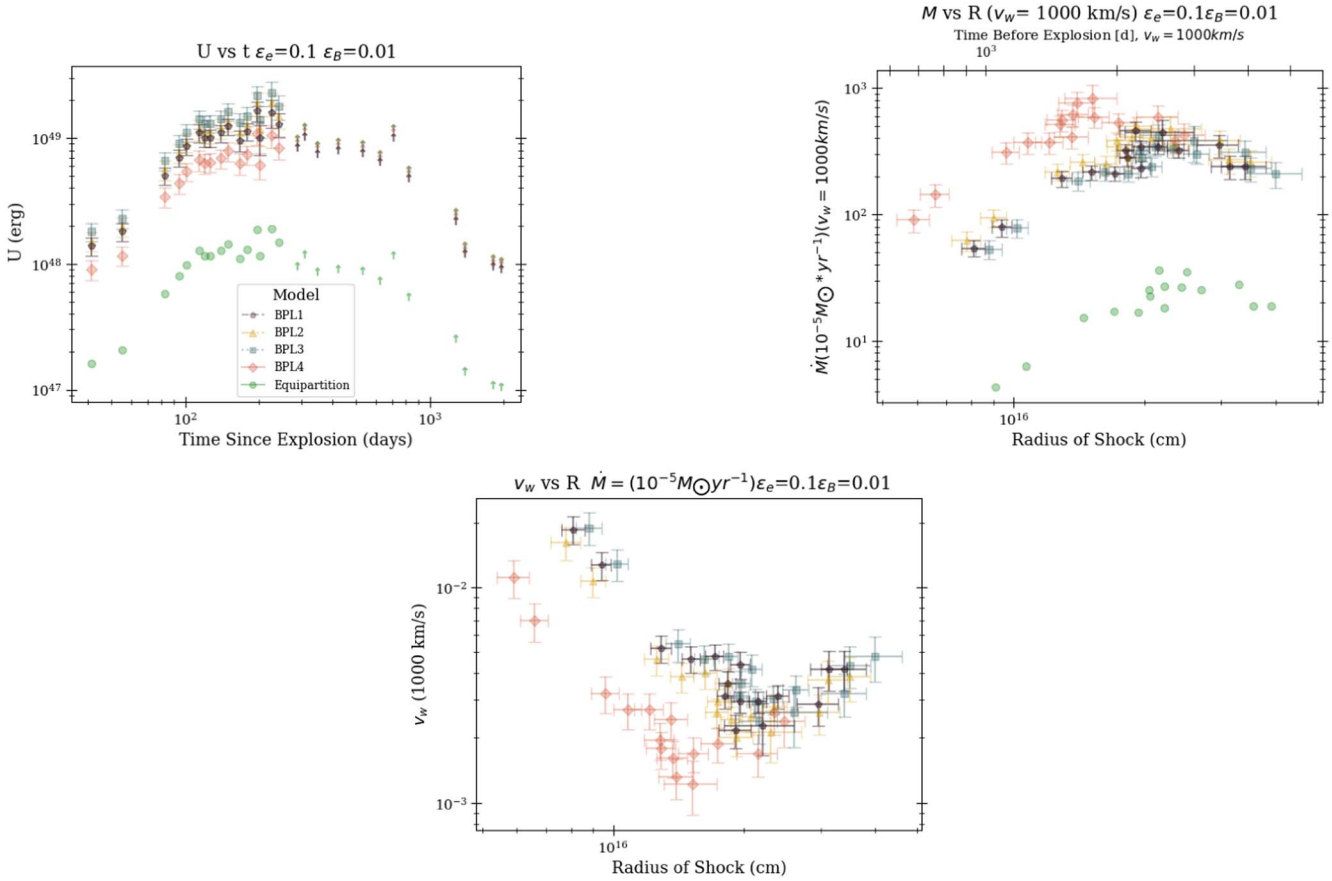

Figure 8. The same as Figure 4, but with all models compared in Section 3.3 and Appendix B. Note that the normalization differs between models, but the overall shape of the evolution remains the same. Purple pentagons: favored model where smoothing parameter is fixed at $s = -1$ and the slope $\alpha_2 = 5/2$ ("BPL1"). Yellow triangles: only smoothing parameter is fixed $s = -1$ ("BPL2"). Blue squares: only slope is fixed $\alpha_2 = 5/2$ ("BPL3"). Pink diamonds: all slopes and s are free to vary ("BPL 4"). Green points: BPL1 in equipartition ($\epsilon_B = \epsilon_e = 1/3$).

Table 2
SED Models Performance Quantified with the F-test and χ^2

Model	χ^2	$M_{\rm params}$	dof	F-Stat 1	$p-$value 1	F-Stat 2	$p-$value 2	F-Stat 3	$p-$value 3	F-Stat 4	$p-$value 4
$\alpha_2 = 5/2$ and $s = -1$ ("BPL1")	70.82	45	49	H_0	H_0	...	...	...	...	...	...
$s = -1$ ("BPL2")	61.89	46	48	1.12	0.34	H_0	H_0	...	...	...	...
$\alpha_2 = 5/2$ ("BPL3")	64.19	46	48	1.08	0.39	...	...	H_0	H_0	...	...
both slopes and s vary ("BPL4")	56.74	47	47	1.20	0.27	1.11	0.36	1.16	0.31	H_0	H_0

Note. "dof" indicates the number of degrees of freedom in the model.

that Model 1 is the preferred fit, following the argument of Occam's Razor. We reject H_0 if the p-value is $p < 5\%$.

Our radio data set of SN 2004C has a number of data points $N_{\rm data} = 94$. The model names are abbreviated with "BPL," referring to their broken power-law shape (Equation (28)), and they represent a joint fit of 28 radio SEDs, which have 56 free parameters (i.e., $\nu_{\rm pk}$, $F_{\rm pk}$, one for each SED) with an additional 1–3 shared parameters between them (slope α_1, slope α_2, and smoothing parameter s). A full discussion of fit parameters and methods is provided in Sections 3.3 and 4.1. For the comparison of BPL2 to BPL3, the number of dof is the same, and we use the χ^2 statistic. We identify BPL1 ($s = -1$, $\alpha_2 = 5/2$) as the favored model by these statistics.

In the Table, Model 1 refers to BPL1, Model 2 refers to BPL2, etc. As an example of how to read the table, for BPL2 (which is Model 2), the column "F – Stat 1" reports the value of the statistics with respect to Model 1, while the column "p – value 1" reports the corresponding p-value.

We also present Figures 7 and 8 as extensions of Figures 3 and 4, respectively, and we provide a version of Figure 5 in Figure 9. These figures contain all four models as well as the equipartition case of BPL1 for ease of comparison. We note that the choice in model can cause a spread among values of

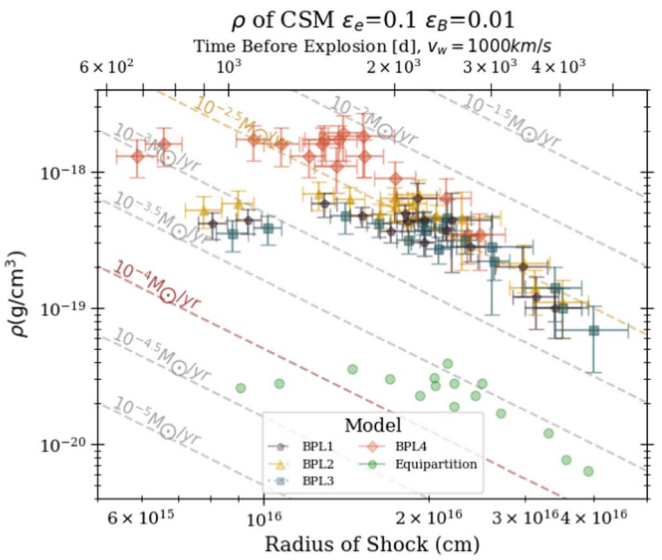

Figure 9. The same as Figure 5, but with all models compared in Section 3.3 and Appendix B. Note that the normalization differs between models, but the overall shape of the evolution remains the same. Purple pentagons: favored model where smoothing parameter is fixed at $s = -1$ and the slope $\alpha_2 = 5/2$ ("BPL1"). Yellow triangles: only smoothing parameter is fixed $s = -1$ ("BPL2"). Blue squares: only slope is fixed $\alpha_2 = 5/2$ ("BPL3"). Pink diamonds: all slopes and s are free to vary ("BPL 4"). Green points: BPL1 in equipartition ($\epsilon_B = \epsilon_e = 1/3$).

physical parameters, but the overall evolution of the inferred parameters remains the same. Additionally, we highlight that the largest variation is associated with the choice of microphysical parameter values ϵ.

Appendix C
Definitions of the Shock Microphysical Parameter ϵ_B (and ϵ_e)

In the radio SN literature, the parameter ϵ_B (and ϵ_e)[18] has been defined in at least four different ways:

$$\frac{B^2}{8\pi} \equiv \epsilon_B \quad \rho_{\rm CSM} v^2 \tag{C1}$$

$$\frac{B^2}{8\pi} \equiv \epsilon_B \rho_{\rm CSM,sh} v^2 = \frac{\Gamma+1}{\Gamma-1}\epsilon_B \rho_{\rm CSM} v^2 \overset{\Gamma=5/3}{=} 4 \times \epsilon_B \rho_{\rm CSM} v^2 \tag{C2}$$

$$\frac{B^2}{8\pi} \equiv \epsilon_B E_{\rm th} = \epsilon_B \frac{1}{2}\rho_{\rm CSM,sh}\left[\left(1 - \frac{\Gamma-1}{\Gamma+1}\right)v\right]^2 \overset{\Gamma=5/3}{=} \frac{9}{8} \times \epsilon_B \rho_{\rm CSM} v^2 \tag{C3}$$

$$\frac{B^2}{8\pi} \equiv \epsilon_B P_2 = \frac{2}{\Gamma+1} \times \epsilon_B \rho_{\rm CSM} v^2 \overset{\Gamma=5/3}{=} \frac{3}{4} \times \epsilon_B \rho_{\rm CSM} v^2 \tag{C4}$$

where B is the magnetic field in the shocked CSM, v is the FS velocity, $\rho_{\rm CSM}$ ($\rho_{\rm CSM,sh}$) is the pre-shock (post-shock) CSM density, Γ is the adiabatic index, $E_{\rm th}$ is the post-shock thermal energy density, and P_2 is the post-shock gas pressure. In other words, ϵ_B is defined as a fraction of different energy densities that, in this paper, we parameterize as $\frac{2}{1+i}\rho_{\rm CSM} v^2$. The corresponding energy is U (Equation (20)).

In the limit of a strong shock scenario, the traditional Rankine–Hugoniot jump conditions apply: $\rho_{\rm CSM,sh} = \frac{\Gamma+1}{\Gamma-1} \times \rho_{\rm CSM}$. For an ideal monatomic gas, $\Gamma = 5/3$, which leads to $\rho_{\rm CSM,sh} = 4 \times \rho_{\rm CSM}$, $E_{\rm th} = \frac{9}{8}\rho_{\rm CSM} v^2$, and $E_{\rm th} = \frac{P_2}{\Gamma-1} = \frac{3}{2}P_2$. In this paper we use $\frac{B^2}{8\pi} = \frac{2}{i+1}\epsilon_B \rho_{\rm CSM} v^2$ as a generic definition, where the parameter i provides flexibility between the different definitions above. When one chooses definition C4, i in our equations becomes conveniently equivalent to the adiabatic index, Γ. Chevalier (1998), Chevalier & Fransson (2017), and related literature adopt the definition of Equation (C1). Definitions C2, C3, C4 have been employed, for example, in Matsuoka & Maeda (2020), Petropoulou et al. (2016), and Ho et al. (2019), respectively. While we present the final inferences on the physical parameters of SN 2004C following Chevalier (1998), we leave the i explicit in our equations to easily visualize the impact of the different definitions on the estimates of the physical parameters.

The obvious consequence of these different definitions of the microphysical parameters is that the inferred values of the physical parameters of the system (e.g., B, R, $\rho_{\rm CSM}$) are not directly comparable among different works, even when the same ϵ_B (and ϵ_e) values are assumed or derived. Derived values of $\dot{M}$ can differ by as much as a factor of $\sim$5 in this way.

In addition, there are two approaches used in the literature for the FS velocity $v \equiv dR/dt$. The first approach utilizes an averaged FS shock velocity since explosion:

$$v \approx \frac{R}{t} \equiv v_{\rm avg}. \tag{C5}$$

A second approach assumes a (local or global) power-law evolution of the FS radius with time $R(t) \propto t^q$:

$$v \equiv dR/dt = q\frac{R}{t}. \tag{C6}$$

At early times, the typical nonrelativistic SN FS is slowly decelerating, and the assumption of a linear evolution of the shock radius with time implicit in Equation (C5) is approximately correct. For SNe in the interaction phase expanding in a power-law density medium for which the self-similar solutions of Chevalier (1982) apply, Equation (C6) provides the exact solution. Following Chevalier (1982), $q = \frac{n-3}{n-s}$, where $\rho_{\rm CSM} \propto r^{-s}$ and the SN ejecta outer density profile is $\rho_{\rm ej} \propto r^{-n}$. For a wind density profile $s = 2$, and a compact massive star (i.e., $n \approx 10$) such as typically assumed for the progenitors of H-stripped SNe, $q = \frac{7}{8}$. Definitions of Equations (C1)–(C4) have been combined with either Equations (C5) or (C6) to solve for the parameter of interest $\rho_{\rm CSM}$ (and, by extension, n_e and $\dot{M}$). For example, Chevalier & Fransson (2006) adopted Equation (C6) for $q = \frac{7}{8}$, while Ho et al. (2019) used the definition of Equation (C4) with the averaged FS velocity $v_{\rm avg}$ of Equation (C5). In this paper we assume a local power-law evolution of the FS radius with time without assuming values for n or s. Instead, we estimate q from a local fit of the FS $R(t)$ inferred from radio data following Equation (17). In our equations, we leave q as a variable, and note that Equation (C6) reduces to Equation (C5) for the special case $q = 1$.

[18] The definitions of ϵ_e can be easily obtained by replacing $E_B = B^2/8\pi$ with E_e, and ϵ_B with ϵ_e in Equations (C1)–(C4).

Appendix D
Radio Data and Calculations

We provide the full radio data set of SN 2004C in Table 3. Similarly, we provide in Tables 4 and 5 the physical parameters calculated using the best-fit parameters inferred from the modeling of the 28 SEDs modeled with BPL1 (Table 1) and Equations (16)–(24). These results are illustrated in Figures 3, 4, and 5. Figure 10 shows the best-fit model BPL1 applied to the full data set.

Table 3
Radio Observations of SN 2004C

Date (MJD)	F_ν 4.9 GHz	F_ν 8.5 GHz	F_ν 15 GHz	F_ν 22 GHz	VLA Config
53027.65		1633 ± 54			BC
53029.41	556 ± 55	1676 ± 42			BC
53030.36				1582 ± 67	BC
53041.36	938 ± 48	1893 ± 35		1856 ± 71	BC
53069.4		4567 ± 38		5205 ± 96	C
53081.15	2326 ± 106	5957 ± 54		5964 ± 167	C
53083.25			8284 ± 153		C
53088.21	3101 ± 78	7012 ± 58	9016 ± 219	6508 ± 164	C
53101.07	3952 ± 102		9739 ± 232		C
53107.14	3678 ± 77	7661 ± 59	10607 ± 234	7196 ± 151	C
53113.08	3387 ± 78	8258 ± 59	10940 ± 256	7017 ± 172	C
53127.14	4473 ± 82	7829 ± 62	10151 ± 219	7651 ± 134	C
53137.18	4927 ± 80	9587 ± 61	9983 ± 247	7216 ± 157	C
53154.16		8175 ± 91	7963 ± 212	6075 ± 130	CD
53165.98	5574 ± 120	7942 ± 58			CD
53166.04			6657 ± 203	4341 ± 91	CD
53183.08	8097 ± 236	8889 ± 109			D
53189.05		7613 ± 122		4267 ± 123	D
53211.98	7808 ± 238	7575 ± 118			D
53212.02			3818 ± 208		D
53212.99				3682 ± 375	D
53228.97	6505 ± 249	7156 ± 130		2654 ± 211	D
53229.02			4488 ± 271		D
53271.84	8873 ± 545	6084 ± 239	2300 ± 201	1722 ± 171	A
53291.59	9423 ± 128	6487 ± 74	3850 ± 181	2816 ± 122	A
53330.67	7796 ± 126	5091 ± 120	2978 ± 198	1749 ± 118	A
53393.2		5273 ± 254			AB
53402.27	8267 ± 233		2270 ± 384	2058 ± 249	AB
53511.47	8620 ± 271				B
53511.9		5486 ± 455	2178 ± 231	1538 ± 166	B
53603.94	7271 ± 367	3968 ± 187	2140 ± 671	1128 ± 658	C
53689.6	10773 ± 365	5355 ± 231	4086 ± 239	2194 ± 238	D
53801.41	5437 ± 139	3356 ± 183	1833 ± 251	1300 ± 135	A
54248.1	3015 ± 116	1586 ± 15		737 ± 131	A
54366.74	1751 ± 163	963 ± 77			AB
54772.5	1226 ± 212	825 ± 100			A
54919.0		740 ± 130			VLBI*
54926.22	1424 ± 78	721 ± 73			B
55781.65	546 ± 60				A

Note. Flux densities are in microjanskys. The measurement on 54919.0 with the VLBA was taken at 8.4 GHz (Section 2). Reported are only the rms uncertainties.

Table 4
Values Plotted in Figures 3–5 for $\epsilon_B = 0.01$ and $\epsilon_e = 0.1$, Using the Favored SED Fit Model BPL1

Days Since Explosion	B (G)	U (erg)	$R_{\rm FS}$ (cm)	n_e (cm^{-3})	$\dot{M}$ ($10^{-5}\,M_\odot$ yr^{-1})	$v_{\rm FS}$ (cm s^{-1})	$\rho_{\rm CSM}$ (g cm^{-3})
41.41–42.36	0.561 ± 0.035	$(1.4 \pm 0.2) \times 10^{48}$	$(8.10 \pm 0.50) \times 10^{15}$	$(2.5 \pm 0.6) \times 10^{5}$	54 ± 8	$(2.26 \pm 0.14) \times 10^{9}$	$(4.1 \pm 0.9) \times 10^{-19}$
55.36	0.508 ± 0.029	$(1.8 \pm 0.3) \times 10^{48}$	$(9.40 \pm 0.50) \times 10^{15}$	$(2.7 \pm 0.5) \times 10^{5}$	79 ± 12	$(1.97 \pm 0.11) \times 10^{9}$	$(4.4 \pm 0.9) \times 10^{-19}$
82.40	0.533 ± 0.030	$(5.0 \pm 0.8) \times 10^{48}$	$(1.29 \pm 0.07) \times 10^{16}$	$(3.5 \pm 0.7) \times 10^{5}$	190 ± 28	$(1.81 \pm 0.10) \times 10^{9}$	$(5.8 \pm 1.2) \times 10^{-19}$
94.15	0.494 ± 0.024	$(7.0 \pm 1.1) \times 10^{48}$	$(1.51 \pm 0.07) \times 10^{16}$	$(2.8 \pm 0.5) \times 10^{5}$	220 ± 29	$(1.85 \pm 0.09) \times 10^{9}$	$(4.7 \pm 0.8) \times 10^{-19}$
101.21	0.454 ± 0.021	$(8.6 \pm 1.3) \times 10^{48}$	$(1.71 \pm 0.08) \times 10^{16}$	$(2.2 \pm 0.4) \times 10^{5}$	210 ± 28	$(1.95 \pm 0.09) \times 10^{9}$	$(3.6 \pm 0.6) \times 10^{-19}$
114.07	0.420 ± 0.024	$(1.1 \pm 0.2) \times 10^{49}$	$(1.96 \pm 0.10) \times 10^{16}$	$(1.8 \pm 0.4) \times 10^{5}$	230 ± 33	$(1.99 \pm 0.10) \times 10^{9}$	$(3.0 \pm 0.6) \times 10^{-19}$
120.14	0.444 ± 0.020	$(1.0 \pm 0.2) \times 10^{49}$	$(1.83 \pm 0.08) \times 10^{16}$	$(2.5 \pm 0.4) \times 10^{5}$	280 ± 40	$(1.76 \pm 0.08) \times 10^{9}$	$(4.3 \pm 0.7) \times 10^{-19}$
126.08	0.450 ± 0.021	$(1.0 \pm 0.2) \times 10^{49}$	$(1.81 \pm 0.08) \times 10^{16}$	$(2.9 \pm 0.5) \times 10^{5}$	320 ± 40	$(1.70 \pm 0.10) \times 10^{9}$	$(4.9 \pm 0.8) \times 10^{-19}$
140.14	0.417 ± 0.019	$(1.1 \pm 0.2) \times 10^{49}$	$(1.96 \pm 0.09) \times 10^{16}$	$(2.6 \pm 0.4) \times 10^{5}$	340 ± 40	$(1.62 \pm 0.07) \times 10^{9}$	$(4.4 \pm 0.7) \times 10^{-19}$
150.18	0.387 ± 0.018	$(1.2 \pm 0.2) \times 10^{49}$	$(2.15 \pm 0.10) \times 10^{16}$	$(2.2 \pm 0.4) \times 10^{5}$	340 ± 40	$(1.66 \pm 0.08) \times 10^{9}$	$(3.7 \pm 0.6) \times 10^{-19}$
167.16	0.406 ± 0.029	$(9.6 \pm 1.8) \times 10^{48}$	$(1.91 \pm 0.16) \times 10^{16}$	$(3.8 \pm 1.1) \times 10^{5}$	460 ± 80	$(1.32 \pm 0.11) \times 10^{9}$	$(6.3 \pm 1.9) \times 10^{-19}$
178.98–179.04	0.315 ± 0.016	$(1.1 \pm 0.2) \times 10^{49}$	$(2.39 \pm 0.14) \times 10^{16}$	$(1.7 \pm 0.4) \times 10^{5}$	320 ± 40	$(1.55 \pm 0.09) \times 10^{9}$	$(2.8 \pm 0.6) \times 10^{-19}$
196.08	0.252 ± 0.023	$(1.6 \pm 0.3) \times 10^{49}$	$(3.14 \pm 0.30) \times 10^{16}$	$(7.4 \pm 2.7) \times 10^{4}$	240 ± 50	$(1.85 \pm 0.18) \times 10^{9}$	$(1.2 \pm 0.5) \times 10^{-19}$
202.05	0.330 ± 0.040	$(1.0 \pm 0.3) \times 10^{49}$	$(2.20 \pm 0.40) \times 10^{16}$	$(2.7 \pm 1.6) \times 10^{5}$	440 ± 120	$(1.28 \pm 0.21) \times 10^{9}$	$(4.4 \pm 2.6) \times 10^{-19}$
224.98–225.99	0.219 ± 0.022	$(1.6 \pm 0.4) \times 10^{49}$	$(3.40 \pm 0.40) \times 10^{16}$	$(6.1 \pm 2.7) \times 10^{4}$	240 ± 50	$(1.77 \pm 0.22) \times 10^{9}$	$(1.0 \pm 0.4) \times 10^{-19}$
241.97–242.02	0.245 ± 0.022	$(1.3 \pm 0.3) \times 10^{49}$	$(2.96 \pm 0.32) \times 10^{16}$	$(1.2 \pm 0.5) \times 10^{5}$	350 ± 70	$(1.42 \pm 0.15) \times 10^{9}$	$(2.0 \pm 0.8) \times 10^{-19}$
284.84	$\leqslant 0.255$	$\geqslant 8.4 \times 10^{48}$	$\geqslant 2.49 \times 10^{16}$	$\leqslant 2.5 \times 10^{5}$	$\leqslant 530$	$\geqslant 1.01 \times 10^{9}$	$\leqslant 4.2 \times 10^{-19}$
304.59	$\leqslant 0.250$	$\geqslant 1.0 \times 10^{49}$	$\geqslant 2.70 \times 10^{16}$	$\leqslant 2.4 \times 10^{5}$	$\leqslant 580$	$\geqslant 1.03 \times 10^{9}$	$\leqslant 3.9 \times 10^{-19}$
343.67	$\leqslant 0.257$	$\geqslant 7.6 \times 10^{48}$	$\geqslant 2.39 \times 10^{16}$	$\leqslant 4.1 \times 10^{5}$	$\leqslant 779$	$\geqslant 8.06 \times 10^{8}$	$\leqslant 6.8 \times 10^{-19}$
406.20–416.27	$\leqslant 0.256$	$\geqslant 8.0 \times 10^{48}$	$\geqslant 2.44 \times 10^{16}$	$\leqslant 5.7 \times 10^{5}$	$\leqslant 1100$	$\geqslant 6.80 \times 10^{8}$	$\leqslant 9.4 \times 10^{-19}$
523.47–523.90	$\leqslant 0.257$	$\geqslant 7.7 \times 10^{48}$	$\geqslant 2.40 \times 10^{16}$	$\leqslant 9.4 \times 10^{5}$	$\leqslant 1800$	$\geqslant 5.30 \times 10^{8}$	$\leqslant 1.5 \times 10^{-18}$
615.94	$\leqslant 0.261$	$\geqslant 6.5 \times 10^{48}$	$\geqslant 2.24 \times 10^{16}$	$\leqslant 1.5 \times 10^{6}$	$\leqslant 2600$	$\geqslant 4.22 \times 10^{8}$	$\leqslant 2.5 \times 10^{-18}$
701.60	$\leqslant 0.250$	$\geqslant 1.0 \times 10^{49}$	$\geqslant 2.69 \times 10^{16}$	$\leqslant 1.3 \times 10^{6}$	$\leqslant 3000$	$\geqslant 4.44 \times 10^{8}$	$\leqslant 2.1 \times 10^{-18}$
813.41	$\leqslant 0.268$	$\geqslant 4.8 \times 10^{48}$	$\geqslant 2.00 \times 10^{16}$	$\leqslant 3.5 \times 10^{6}$	$\leqslant 4700$	$\geqslant 2.84 \times 10^{8}$	$\leqslant 5.9 \times 10^{-18}$
1260.10	$\leqslant 0.286$	$\geqslant 2.2 \times 10^{48}$	$\geqslant 1.47 \times 10^{16}$	$\leqslant 1.8 \times 10^{7}$	$\leqslant 13000$	$\geqslant 1.35 \times 10^{8}$	$\leqslant 2.9 \times 10^{-17}$
1378.74	$\leqslant 0.302$	$\geqslant 1.2 \times 10^{48}$	$\geqslant 1.16 \times 10^{16}$	$\leqslant 3.8 \times 10^{7}$	$\leqslant 17000$	$\geqslant 9.80 \times 10^{7}$	$\leqslant 6.3 \times 10^{-17}$
1785.5	$\leqslant 0.308$	$\geqslant 9.6 \times 10^{47}$	$\geqslant 1.06 \times 10^{16}$	$\leqslant 8.0 \times 10^{7}$	$\leqslant 30000$	$\geqslant 6.90 \times 10^{7}$	$\leqslant 1.3 \times 10^{-16}$
1931.0	…	…	$3.8^{+0.6}_{-1.0} \times 10^{17}$	…	…	…	…
1938.22	$\leqslant 0.309$	$\geqslant 9.2 \times 10^{47}$	$\geqslant 1.04 \times 10^{16}$	$\leqslant 9.8 \times 10^{7}$	$\leqslant 36000$	$\geqslant 6.25 \times 10^{7}$	$\leqslant 1.6 \times 10^{-16}$

Note. $\dot{M}$ is calculated assuming a wind velocity of 1000 km s^{-1}. The measurement taken 1931 days post-explosion is the radius measurement from VLBI (described in Section 2).

Table 5
Values Plotted in Figures 3–5 for Equipartition $\epsilon_B = \epsilon_e = \frac{1}{3}$, Using the Favored SED Fit Model BPL1

Days Since Explosion	B (G)	U (erg)	$R_{\rm FS}$ (cm)	n_e (cm^{-3})	$\dot{M}$ ($10^{-5}\,M_\odot$ yr^{-1})	$v_{\rm FS}$ (cm s^{-1})	$\rho_{\rm CSM}$ (g cm^{-3})
41.41–42.36	0.91 ± 0.06	$(1.60 \pm 0.25) \times 10^{47}$	$(9.10 \pm 0.50) \times 10^{15}$	$(1.5 \pm 0.3) \times 10^{4}$	4.3 ± 0.7	$(2.55 \pm 0.15) \times 10^{9}$	$(2.6 \pm 0.6) \times 10^{-20}$
55.36	0.83 ± 0.05	$(2.08 \pm 0.31) \times 10^{47}$	$(1.07 \pm 0.06) \times 10^{16}$	$(1.6 \pm 0.3) \times 10^{4}$	6.3 ± 0.9	$(2.23 \pm 0.12) \times 10^{9}$	$(2.8 \pm 0.6) \times 10^{-20}$
82.40	0.87 ± 0.05	$(5.80 \pm 0.90) \times 10^{47}$	$(1.45 \pm 0.08) \times 10^{16}$	$(2.2 \pm 0.5) \times 10^{4}$	15 ± 2.2	$(2.04 \pm 0.11) \times 10^{9}$	$(3.6 \pm 0.8) \times 10^{-20}$
94.15	0.81 ± 0.04	$(8.00 \pm 1.20) \times 10^{47}$	$(1.70 \pm 0.08) \times 10^{16}$	$(1.7 \pm 0.3) \times 10^{4}$	17 ± 2.3	$(2.09 \pm 0.10) \times 10^{9}$	$(3.0 \pm 0.5) \times 10^{-20}$
101.21	0.74 ± 0.03	$(9.90 \pm 1.40) \times 10^{47}$	$(1.93 \pm 0.08) \times 10^{16}$	$(1.3 \pm 0.2) \times 10^{4}$	17 ± 2.1	$(2.21 \pm 0.10) \times 10^{9}$	$(2.3 \pm 0.4) \times 10^{-20}$
114.07	0.69 ± 0.04	$(1.28 \pm 0.20) \times 10^{48}$	$(2.22 \pm 0.11) \times 10^{16}$	$(1.1 \pm 0.2) \times 10^{4}$	18 ± 2.6	$(2.25 \pm 0.11) \times 10^{9}$	$(1.9 \pm 0.4) \times 10^{-20}$
120.14	0.72 ± 0.03	$(1.15 \pm 0.17) \times 10^{48}$	$(2.06 \pm 0.09) \times 10^{16}$	$(1.6 \pm 0.2) \times 10^{4}$	23 ± 2.8	$(1.99 \pm 0.09) \times 10^{9}$	$(2.7 \pm 0.4) \times 10^{-20}$
126.08	0.73 ± 0.03	$(1.16 \pm 0.17) \times 10^{48}$	$(2.05 \pm 0.09) \times 10^{16}$	$(1.8 \pm 0.3) \times 10^{4}$	26 ± 3.2	$(1.88 \pm 0.08) \times 10^{9}$	$(3.1 \pm 0.5) \times 10^{-20}$
140.14	0.68 ± 0.03	$(1.27 \pm 0.18) \times 10^{48}$	$(2.22 \pm 0.10) \times 10^{16}$	$(1.7 \pm 0.3) \times 10^{4}$	27 ± 3.4	$(1.83 \pm 0.08) \times 10^{9}$	$(2.8 \pm 0.4) \times 10^{-20}$
150.18	0.63 ± 0.03	$(1.43 \pm 0.21) \times 10^{48}$	$(2.43 \pm 0.11) \times 10^{16}$	$(1.4 \pm 0.2) \times 10^{4}$	27 ± 3.4	$(1.87 \pm 0.09) \times 10^{9}$	$(2.3 \pm 0.4) \times 10^{-20}$
167.16	0.66 ± 0.05	$(1.10 \pm 0.19) \times 10^{48}$	$(2.16 \pm 0.18) \times 10^{16}$	$(2.3 \pm 0.7) \times 10^{4}$	36 ± 6	$(1.50 \pm 0.13) \times 10^{9}$	$(3.9 \pm 1.2) \times 10^{-20}$
178.98–179.04	0.51 ± 0.03	$(1.30 \pm 0.20) \times 10^{48}$	$(2.70 \pm 0.16) \times 10^{16}$	$(1.0 \pm 0.2) \times 10^{4}$	$25. \pm 3.4$	$(1.75 \pm 0.10) \times 10^{9}$	$(1.7 \pm 0.4) \times 10^{-20}$
196.08	0.41 ± 0.04	$(1.89 \pm 0.34) \times 10^{48}$	$(3.55 \pm 0.34) \times 10^{16}$	(4.6 ± 1.7)e+03	19 ± 4	$(2.10 \pm 0.20) \times 10^{9}$	$(7.7 \pm 2.8) \times 10^{-21}$
202.05	0.54 ± 0.07	$(1.15 \pm 0.30) \times 10^{48}$	$(2.50 \pm 0.40) \times 10^{16}$	$(1.7 \pm 1.0) \times 10^{4}$	35 ± 10	$(1.44 \pm 0.23) \times 10^{9}$	$(2.8 \pm 1.6) \times 10^{-20}$
224.98–225.99	0.35 ± 0.03	$(1.90 \pm 0.40) \times 10^{48}$	$(3.90 \pm 0.50) \times 10^{16}$	(3.8 ± 1.7)e+03	19 ± 4	$(2.00 \pm 0.24) \times 10^{9}$	$(6.4 \pm 2.8) \times 10^{-21}$
241.97–242.02	0.39 ± 0.03	$(1.49 \pm 0.29) \times 10^{48}$	$(3.30 \pm 0.40) \times 10^{16}$	(7.5 ± 2.9)e+03	28 ± 5	$(1.60 \pm 0.17) \times 10^{9}$	$(1.2 \pm 0.5) \times 10^{-20}$
284.84	$\leqslant 0.41$	$\geqslant 9.72 \times 10^{47}$	$\geqslant 2.82 \times 10^{16}$	$\leqslant 1.5 \times 10^{4}$	$\leqslant 42$	$\geqslant 1.15 \times 10^{9}$	$\leqslant 2.6 \times 10^{-20}$
304.59	$\leqslant 0.40$	$\geqslant 1.19 \times 10^{48}$	$\geqslant 3.06 \times 10^{16}$	$\leqslant 1.5 \times 10^{4}$	$\leqslant 46$	$\geqslant 1.16 \times 10^{9}$	$\leqslant 2.4 \times 10^{-20}$
343.67	$\leqslant 0.42$	$\geqslant 8.72 \times 10^{47}$	$\geqslant 2.70 \times 10^{16}$	$\leqslant 2.6 \times 10^{4}$	$\leqslant 62$	$\geqslant 9.11 \times 10^{8}$	$\leqslant 4.2 \times 10^{-20}$
406.20–416.27	$\leqslant 0.41$	$\geqslant 9.23 \times 10^{47}$	$\geqslant 2.76 \times 10^{16}$	$\leqslant 3.5 \times 10^{4}$	$\leqslant 90$	$\geqslant 7.69 \times 10^{8}$	$\leqslant 5.9 \times 10^{-20}$
523.47–523.90	$\leqslant 0.41$	$\geqslant 8.82 \times 10^{47}$	$\geqslant 2.71 \times 10^{16}$	$\leqslant 5.9 \times 10^{4}$	$\leqslant 140$	$\geqslant 6.00 \times 10^{8}$	$\leqslant 9.8 \times 10^{-20}$
615.94	$\leqslant 0.42$	$\geqslant 7.43 \times 10^{47}$	$\geqslant 2.54 \times 10^{16}$	$\leqslant 9.5 \times 10^{4}$	$\leqslant 200$	$\geqslant 4.77 \times 10^{8}$	$\leqslant 1.5 \times 10^{-19}$
701.60	$\leqslant 0.41$	$\geqslant 1.17 \times 10^{48}$	$\geqslant 3.04 \times 10^{16}$	$\leqslant 8.0 \times 10^{4}$	$\leqslant 250$	$\geqslant 5.01 \times 10^{8}$	$\leqslant 1.3 \times 10^{-19}$

Table 5
(Continued)

Days Since Explosion	B (G)	U (erg)	$R_{\rm FS}$ (cm)	n_e (cm^{-3})	$\dot{M}$ (10^{-5} $M_\odot$ yr^{-1})	$v_{\rm FS}$ (cm s^{-1})	$\rho_{\rm CSM}$ (g cm^{-3})
813.41	$\leqslant 0.43$	$\geqslant 5.53 \times 10^{47}$	$\geqslant 2.26 \times 10^{16}$	$\leqslant 2.2 \times 10^{5}$	$\leqslant 380$	$\geqslant 3.22 \times 10^{8}$	$\leqslant 3.6 \times 10^{-19}$
1260.10	$\leqslant 0.46$	$\geqslant 2.56 \times 10^{47}$	$\geqslant 1.67 \times 10^{16}$	$\leqslant 1.1 \times 10^{6}$	$\leqslant 1000$	$\geqslant 1.53 \times 10^{8}$	$\leqslant 1.8 \times 10^{-18}$
1378.74	$\leqslant 0.49$	$\geqslant 1.40 \times 10^{47}$	$\geqslant 1.31 \times 10^{16}$	$\leqslant 2.3 \times 10^{6}$	$\leqslant 1400$	$\geqslant 1.11 \times 10^{8}$	$\leqslant 3.9 \times 10^{-18}$
1785.5	$\leqslant 0.50$	$\geqslant 1.11 \times 10^{47}$	$\geqslant 1.20 \times 10^{16}$	$\leqslant 5.0 \times 10^{6}$	$\leqslant 2400$	$\geqslant 7.80 \times 10^{7}$	$\leqslant 8.3 \times 10^{-18}$
1931.0	...	...	$3.8^{+0.6}_{-1.0} \times 10^{17}$	...	...	...	...
1938.22	$\leqslant 0.50$	$\geqslant 1.06 \times 10^{47}$	$\geqslant 1.18 \times 10^{16}$	$\leqslant 6.1 \times 10^{6}$	$\leqslant 2900$	$\geqslant 7.07 \times 10^{7}$	$\leqslant 1.0 \times 10^{-17}$

Note. $\dot{M}$ assumes a wind velocity of 1000 km s^{-1}. The measurement taken 1931 days post-explosion is the radius measurement from VLBI (described in Section 2).

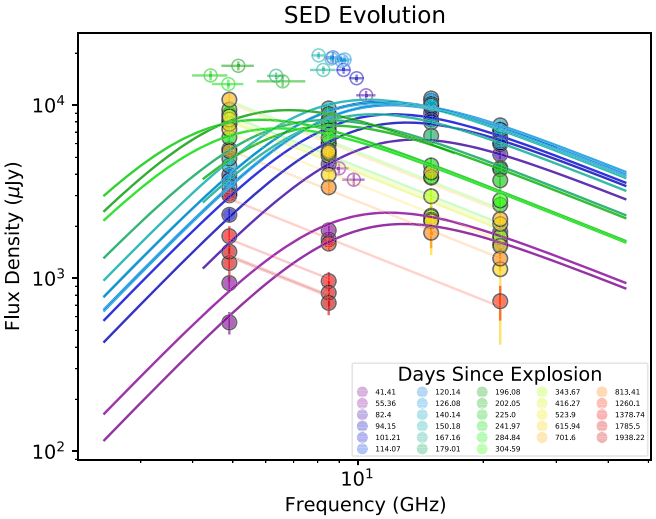

Figure 10. The full spectral energy distribution (SED) evolution of SN 2004C, with data grouped in SED following the criterion of time range of acquisition $\delta t/t < 0.025$. Solid points: radio data of SN 2004C (provided in Table 3). Solid lines: our favored model BPL1, a BPL with smoothing parameter s fixed to -1 and optically thick slope α_2 fixed to 5/2. Hollow points: the asymptotic intercept of the thick and thin slopes of the BPL, identified as $F_{\rm br}$ and $\nu_{\rm br}$ in Table 1 and used in our calculations of the physical parameters. At later times, the SED peak migrates to frequencies too low to capture both sides of the SED. In this case, a single power law is fit to the SED, and the peak becomes a flux density (frequency) lower limit (upper limit) propagated through the physical parameters.

ORCID iDs

Lindsay DeMarchi https://orcid.org/0000-0003-4587-2366
R. Margutti https://orcid.org/0000-0003-4768-7586
A. Brunthaler https://orcid.org/0000-0003-4468-761X
D. Milisavljevic https://orcid.org/0000-0002-0763-3885
Michael F. Bietenholz https://orcid.org/0000-0002-0592-4152
C. Stauffer https://orcid.org/0000-0001-8769-4591
D. Brethauer https://orcid.org/0000-0001-6415-0903
D. Coppejans https://orcid.org/0000-0001-5126-6237
K. Auchettl https://orcid.org/0000-0002-4449-9152
K. D. Alexander https://orcid.org/0000-0002-8297-2473
C. D. Kilpatrick https://orcid.org/0000-0002-5740-7747
Joe S. Bright https://orcid.org/0000-0002-7735-5796
L. Z. Kelley https://orcid.org/0000-0002-6625-6450
Michael C. Stroh https://orcid.org/0000-0002-3019-4577
W. V. Jacobson-Galán https://orcid.org/0000-0003-1103-3409

References

Alexander, K. D., van Velzen, S., Horesh, A., & Zauderer, B. A. 2020, SSRv, 216, 81
Anderson, J. P., Pessi, P. J., Dessart, L., et al. 2018, A&A, 620, A67
Arcavi, I., Gal-Yam, A., Yaron, O., et al. 2011, ApJL, 742, L18
Asplund, M., Grevesse, N., Sauval, A. J., & Scott, P. 2009, ARA&A, 47, 481
Balasubramanian, A., Corsi, A., Polisensky, E., Clarke, T. E., & Kassim, N. E. 2021, ApJ, 923, 32
Bellm, E. C., Kulkarni, S. R., Graham, M. J., et al. 2019, PASP, 131, 018002
Benetti, S., Zampieri, L., Pastorello, A., et al. 2018, MNRAS, 476, 261
Berger, E., Kulkarni, S. R., & Chevalier, R. A. 2002, ApJL, 577, L5
Bhirombhakdi, K., Chornock, R., Miller, A. A., et al. 2019, MNRAS, 488, 3783
Bietenholz, M. F., Bartel, N., Argo, M., et al. 2021, ApJ, 908, 75
Bietenholz, M. F., De Colle, F., Granot, J., Bartel, N., & Soderberg, A. M. 2014, MNRAS, 440, 821
Blondin, S., & Tonry, J. L. 2007, ApJ, 666, 1024
Brethauer, D., Margutti, R., Milisavljevic, D., et al. 2022, arXiv:2206.00842
Bruch, R. J., Gal-Yam, A., Schulze, S., et al. 2021, ApJ, 912, 46
Chen, T. W., Brennan, S. J., Wesson, R., et al. 2021, arXiv:2109.07942
Chen, T. W., Inserra, C., Fraser, M., et al. 2018, ApJL, 867, L31
Chevalier, R. A. 1982, ApJ, 258, 790
Chevalier, R. A. 1998, ApJ, 499, 810
Chevalier, R. A., & Fransson, C. 2006, ApJ, 651, 381
Chevalier, R. A., & Fransson, C. 2017, in Thermal and Non-thermal Emission from Circumstellar Interaction, ed. A. W. Alsabti & P. Murdin (New York: Springer), 875
Chugai, N. N., & Chevalier, R. A. 2006, ApJ, 641, 1051
Corsi, A., Gal-Yam, A., Kulkarni, S. R., et al. 2016, ApJ, 830, 42
Corsi, A., Ofek, E. O., Gal-Yam, A., et al. 2014, ApJ, 782, 42
Crockett, R. M., Eldridge, J. J., Smartt, S. J., et al. 2008, MNRAS, 391, L5
Crowther, P. A. 2007, ARA&A, 45, 177
Davidson, K. 2020, Galax, 8, 10
de Jager, C., Nieuwenhuijzen, H., & van der Hucht, K. A. 1988, A&AS, 72, 259
Diesing, R., & Caprioli, D. 2021, ApJ, 922, 1
Dong, D. Z., Hallinan, G., Nakar, E., et al. 2021, Sci, 373, 1125
Dudley, C. C., & Fischer, J. 2004, CBET, 57, 1
Dwarkadas, V. V., Dewey, D., & Bauer, F. 2010, MNRAS, 407, 812
Fey, A. L., Ma, C., Arias, E. F., et al. 2004, AJ, 127, 3587
Filippenko, A. V. 1997, ARA&A, 35, 309
Folatelli, G., Bersten, M. C., Benvenuto, O. G., et al. 2014, ApJL, 793, L22
Folatelli, G., Bersten, M. C., Kuncarayakti, H., et al. 2015, ApJ, 811, 147
Foley, R. J., Berger, E., Fox, O., et al. 2011, ApJ, 732, 32
Fox, O. D., Azalee Bostroem, K., Van Dyk, S. D., et al. 2014, ApJ, 790, 17
Fraser, M., Magee, M., Kotak, R., et al. 2013, ApJL, 779, L8
Fraser, M., Stritzinger, M. D., Brennan, S. J., et al. 2021, arXiv:2108.07278
Fuller, J., & Ro, S. 2018, MNRAS, 476, 1853
Gal-Yam, A., Arcavi, I., Ofek, E. O., et al. 2014, Natur, 509, 471
Gal-Yam, A., Yaron, O., Pastorello, A., et al. 2021, TNSAN, 76, 1
Gayley, K. G. 1995, ApJ, 454, 410
Gilkis, A., & Arcavi, I. 2022, MNRAS, 511, 691
Gomez, S., Berger, E., Nicholl, M., et al. 2019, ApJ, 881, 87
Graham, M. J., Kulkarni, S. R., Bellm, E. C., et al. 2019, PASP, 131, 078001
Granot, J., & Sari, R. 2002, ApJ, 568, 820
Groh, J. H. 2014, A&A, 572, L11
Groh, J. H., Meynet, G., & Ekström, S. 2013, A&A, 550, L7

Gutiérrez, C. P., Bersten, M. C., Orellana, M., et al. 2021, MNRAS, 504, 4907
Heger, A., Fryer, C. L., Woosley, S. E., Langer, N., & Hartmann, D. H. 2003, ApJ, 591, 288
Ho, A. Y. Q., Phinney, E. S., Ravi, V., et al. 2019, ApJ, 871, 73
Hosseinzadeh, G., Berger, E., Metzger, B. D., et al. 2022, ApJ, 933, 14
Humphreys, R. M., Davidson, K., Van Dyk, S. D., & Gordon, M. S. 2017, ApJ, 848, 86
Humphreys, R. M., Stangl, S., Gordon, M. S., Davidson, K., & Grammer, S. H. 2019, AJ, 157, 22
Jacobson-Galán, W., Dessart, L., Jones, D., et al. 2022, ApJ, 924, 15
Jacobson-Galán, W. V., Margutti, R., Kilpatrick, C. D., et al. 2020, ApJ, 898, 166
Jacobson-Galán, W. V., Margutti, R., Kilpatrick, C. D., et al. 2021, ApJL, 908, L32
Jin, H., Yoon, S.-C., & Blinnikov, S. 2021, ApJ, 910, 68
Kamble, A., Margutti, R., Soderberg, A. M., et al. 2016, ApJ, 818, 111
Kelly, P. L., & Kirshner, R. P. 2012, ApJ, 759, 107
Kettenis, M., van Langevelde, H. J., Reynolds, C., & Cotton, B. 2006, in ASP Conf. Ser. 351, Astronomical Data Analysis Software and Systems XV, ed. C. Gabriel et al. (San Francisco, CA: ASP), 497
Kilpatrick, C. D., Coulter, D. A., Foley, R. J., et al. 2022, ApJ, 936, 111
Kilpatrick, C. D., Foley, R. J., Abramson, L. E., et al. 2017, MNRAS, 465, 4650
Kotak, R., & Vink, J. S. 2006, A&A, 460, L5
Kuncarayakti, H., Maeda, K., Ashall, C. J., et al. 2018, ApJL, 854, L14
Kundu, E., Lundqvist, P., Sorokina, E., et al. 2019, ApJ, 875, 17
Law, N. M., Kulkarni, S. R., Dekany, R. G., et al. 2009, PASP, 121, 1395
Leung, S.-C., & Fuller, J. 2020, ApJ, 900, 99
Leung, S.-C., Fuller, J., & Nomoto, K. 2021a, ApJ, 915, 80
Leung, S.-C., Nomoto, K., & Blinnikov, S. 2019, ApJ, 887, 72
Leung, S.-C., Wu, S., & Fuller, J. 2021b, ApJ, 923, 41
Lunnan, R., Fransson, C., Vreeswijk, P. M., et al. 2018, NatAs, 2, 887
Maeda, K., Chandra, P., Matsuoka, T., et al. 2021, ApJ, 918, 34
Maeda, K., Hattori, T., Milisavljevic, D., et al. 2015, ApJ, 807, 35
Margutti, R., Kamble, A., Milisavljevic, D., et al. 2017, ApJ, 835, 140
Margutti, R., Milisavljevic, D., Soderberg, A. M., et al. 2014, ApJ, 780, 21
Marshall, J. R., van Loon, J. T., Matsuura, M., et al. 2004, MNRAS, 355, 1348
Matheson, T., Challis, P., Kirshner, R., & Berlind, P. 2004, CBET, 57, 2
Matsuoka, T., & Maeda, K. 2020, ApJ, 898, 158
Mauerhan, J., Williams, G. G., Smith, N., et al. 2014, MNRAS, 442, 1166
Mauerhan, J. C., Filippenko, A. V., Zheng, W., et al. 2018, MNRAS, 478, 5050
Mauerhan, J. C., Smith, N., Filippenko, A. V., et al. 2013, MNRAS, 430, 1801
Mauron, N., & Josselin, E. 2011, A&A, 526, A156
Meikle, W. P. S., Mattila, S., Carter, D., & Smith, R. J. 2004, IAU Circ., 8270, 2
Milisavljevic, D., Margutti, R., Kamble, A., et al. 2015, ApJ, 815, 120
Milisavljevic, D., Margutti, R., Soderberg, A. M., et al. 2013, ApJ, 767, 71
Newville, M., Stensitzki, T., Allen, D. B., & Ingargiola, A. 2014, LMFIT: Non-Linear Least-Square Minimization and Curve-Fitting for Python v0.8.0, Zenodo, doi:10.5281/zenodo.11813
Ofek, E. O., Sullivan, M., Cenko, S. B., et al. 2013, Natur, 494, 65
Ofek, E. O., Sullivan, M., Shaviv, N. J., et al. 2014, ApJ, 789, 104
Orellana, M., Bersten, M. C., Folatelli, G., et al. 2018, BAAA, 60, 26
Owocki, S. P., Gayley, K. G., & Shaviv, N. J. 2004, ApJ, 616, 525
Pacholczyk, A. G. 1970, Radio Astrophysics. Nonthermal Processes in Galactic and Extragalactic Sources (San Francisco, CA: Freeman), 232
Pastorello, A., Cappellaro, E., Inserra, C., et al. 2013, ApJ, 767, 1
Perley, D. A., Sollerman, J., Schulze, S., et al. 2022, ApJ, 927, 180
Petropoulou, M., Kamble, A., & Sironi, L. 2016, MNRAS, 460, 44
Piro, A. L., Muhleisen, M., Arcavi, I., et al. 2017, ApJ, 846, 94
Prentice, S. J., Maguire, K., Boian, I., et al. 2020, MNRAS, 499, 1450
Prieto, J. L., Brimacombe, J., Drake, A. J., & Howerton, S. 2013, ApJL, 763, L27
Pursiainen, M., Leloudas, G., Paraskeva, E., et al. 2022, arXiv:2202.01635
Quataert, E., & Shiode, J. 2012, MNRAS, 423, L92
Roming, P. W. A., Pritchard, T. A., Brown, P. J., et al. 2009, ApJL, 704, L118
Rybicki, G. B., & Lightman, A. P. 1986, Radiative Processes in Astrophysics (Weinheim: Wiley-VCH), 8
Ryder, S. D., Murrowood, C. E., & Stathakis, R. A. 2006, MNRAS, 369, L32
Ryder, S. D., Sadler, E. M., Subrahmanyan, R., et al. 2004, MNRAS, 349, 1093
Ryder, S. D., Van Dyk, S. D., Fox, O. D., et al. 2018, ApJ, 856, 83
Salas, P., Bauer, F. E., Stockdale, C., & Prieto, J. L. 2013, MNRAS, 428, 1207
Schinzel, F. K., Taylor, G. B., Stockdale, C. J., Granot, J., & Ramirez-Ruiz, E. 2009, ApJ, 691, 1380
Seaquist, E. R., Krogulec, M., & Taylor, A. R. 1993, ApJ, 410, 260
Shivvers, I., Modjaz, M., Zheng, W., et al. 2017, PASP, 129, 054201
Smartt, S. J. 2015, PASA, 32, e016
Smith, N. 2014, ARA&A, 52, 487
Smith, N., & Arnett, W. D. 2014, ApJ, 785, 82
Smith, N., Miller, A., Li, W., et al. 2010, AJ, 139, 1451
Smith, N., & Owocki, S. P. 2006, ApJL, 645, L45
Soderberg, A. 2007, PhD thesis, California Institute of Technology
Soderberg, A. M., Brunthaler, A., Nakar, E., Chevalier, R. A., & Bietenholz, M. F. 2010a, ApJ, 725, 922
Soderberg, A. M., Chakraborti, S., Pignata, G., et al. 2010b, Natur, 463, 513
Soderberg, A. M., Chevalier, R. A., Kulkarni, S. R., & Frail, D. A. 2006, ApJ, 651, 1005
Soderberg, A. M., Frail, D. A., & Wieringa, M. H. 2004, ApJL, 607, L13
Soderberg, A. M., Margutti, R., Zauderer, B. A., et al. 2012, ApJ, 752, 78
Soderberg, A. M., Nakar, E., Berger, E., & Kulkarni, S. R. 2006c, ApJ, 638, 930
Soderberg, A. M., Nakar, E., Cenko, S. B., et al. 2007, ApJ, 661, 982
Sravan, N., Marchant, P., & Kalogera, V. 2019, ApJ, 885, 130
Sravan, N., Marchant, P., Kalogera, V., & Margutti, R. 2018, ApJL, 852, L17
Sravan, N., Marchant, P., Kalogera, V., Milisavljevic, D., & Margutti, R. 2020, ApJ, 903, 70
Stroh, M. C., Terreran, G., Coppejans, D. L., et al. 2021, ApJL, 923, L24
Strotjohann, N. L., Ofek, E. O., Gal-Yam, A., et al. 2021, ApJ, 907, 99
Tartaglia, L., Fraser, M., Sand, D. J., et al. 2017, ApJL, 836, L12
Terreran, G., Margutti, R., Bersier, D., et al. 2019, ApJ, 883, 147
Tully, R. B., Courtois, H. M., Dolphin, A. E., et al. 2013, AJ, 146, 86
Tully, R. B., Rizzi, L., Shaya, E. J., et al. 2009, AJ, 138, 323
van Loon, J. T., Cioni, M. R. L., Zijlstra, A. A., & Loup, C. 2005, A&A, 438, 273
Weiler, K. W., Panagia, N., Montes, M. J., & Sramek, R. A. 2002, ARA&A, 40, 387
Woosley, S. E. 2017, ApJ, 836, 244
Woosley, S. E., & Heger, A. 2015, ApJ, 810, 34
Wu, S., & Fuller, J. 2021, ApJ, 906, 3
Yan, L., Lunnan, R., Perley, D. A., et al. 2017, ApJ, 848, 6
Yang, Y.-P., & Zhang, B. 2018, ApJL, 864, L16
Yao, Y., Ho, A. Y. Q., Medvedev, P., et al. 2021, ApJ, 934, 104
Yaron, O., & Gal-Yam, A. 2012, PASP, 124, 668
Yoon, S.-C., Dessart, L., & Clocchiatti, A. 2017, ApJ, 840, 10
Zapartas, E., de Mink, S. E., Izzard, R. G., et al. 2017, A&A, 601, A29